Journal of Structural Biology 212 (2020) 107616

Contents lists available at ScienceDirect

Journal of Structural Biology

journal homepage: www.elsevier.com/locate/yjsbi

Heterogeneity of the osteocyte lacuno-canalicular network architecture and material characteristics across different tissue types in healing bone

Victoria Schemenz[a,1], André Gjardy[a,1], Fereshteh F. Chamasemani[b], Andreas Roschger[a,c], Paul Roschger[d], Paul Zaslansky[e], Lukas Helfen[f,g], Manfred Burghammer[h], Peter Fratzl[a], Richard Weinkamer[a], Roland Brunner[b], Bettina M. Willie[i], Wolfgang Wagermaier[a,*]

[a] Max Planck Institute of Colloids and Interfaces, Department of Biomaterials, Am Mühlenberg 1, 14476 Potsdam, Germany
[b] Materials Center Leoben Forschung GmbH, 8700 Leoben, Austria
[c] Paris-Lodron-University of Salzburg, Department of Chemistry and Physics of Materials, Salzburg, Austria
[d] Ludwig Boltzmann Institute of Osteology at Hanusch Hospital of ÖGK and AUVA Trauma Centre Meidling, 1st Medical Department, Hanusch Hospital, Vienna, Austria
[e] Department for Restorative and Preventive Dentistry, Charité-Universitaetsmedizin Berlin, Berlin 14197, Germany
[f] Institute for Photon Science and Synchrotron Radiation, Karlsruhe Institute of Technology, D-76021 Karlsruhe, Germany
[g] Institut Laue-Langevin, CS 20156, 38042 Grenoble Cedex 9, France
[h] European Synchrotron Radiation Facility, Grenoble, France
[i] Research Centre, Shriners Hospitals for Children-Canada, Department of Pediatric Surgery, McGill University, 1003 Decarie Blvd, Montreal, Quebec H4A 0A9, Canada

ARTICLE INFO

Keywords:
Endochondral ossification
Lacuno-canalicular network
qBEI
CLSM
SAXS
μCT

ABSTRACT

Various tissue types, including fibrous connective tissue, bone marrow, cartilage, woven and lamellar bone, coexist in healing bone. Similar to most bone tissue type, healing bone contains a lacuno-canalicular network (LCN) housing osteocytes. These cells are known to orchestrate bone remodeling in healthy bone by sensing mechanical strains and translating them into biochemical signals. The structure of the LCN is hypothesized to influence mineralization processes. Hence, the aim of the present study was to visualize and match spatial variations in the LCN topology with mineral characteristics, within and at the interfaces of the different tissue types that comprise healing bone. We applied a correlative multi-method approach to visualize the LCN architecture and quantify mineral particle size and orientation within healing femoral bone in a mouse osteotomy model (26 weeks old C57BL/6 mice). This approach revealed structural differences across several length scales during endochondral ossification within the following regions: calcified cartilage, bony callus, cortical bone and a transition zone between the cortical and callus region analyzed 21 days after the osteotomy. In this transition zone, we observed a continuous convergence of mineral characteristics and osteocyte lacunae shape as well as discontinuities in the lacunae volume and LCN connectivity. The bony callus exhibits a 34% higher lacunae number density and 40% larger lacunar volume compared to cortical bone. The presented correlations between LCN architecture and mineral characteristics improves our understanding of how bone develops during healing and may indicate a contribution of osteocytes to bone (re)modeling.

1. Introduction

The capacity to regenerate makes bone one of the most remarkable tissues in our body. The process of self-repair (healing) after fracture occurs predominantly by indirect healing, also known as secondary healing, which includes a combination of endochondral and intramembranous bone formation (Gerstenfeld et al., 2006). Secondary healing starts with an inflammatory phase, in which dead material is removed from the fracture zone and a hematoma is formed. Thereafter structural regeneration takes place, where mechanical stabilization is supported by the emergence of a callus consisting initially of fibrous connective tissue that is substituted by cartilage (Dimitriou et al., 2005). This soft callus is then replaced by a bony callus (Al-Aql et al., 2008; Marsell and Einhorn, 2012). The initially formed mineralized tissue exhibits a rather unordered structure – similar to woven bone (Reznikov et al., 2014) – and its mechanical properties are still inferior to the pre-fractured cortical bone. The woven bone structure serves as a scaffold on which groups of osteoblasts can align and collectively form

* Corresponding author.
E-mail address: wolfgang.wagermaier@mpikg.mpg.de (W. Wagermaier).
[1] These authors contributed equally to this work.

https://doi.org/10.1016/j.jsb.2020.107616
Received 15 May 2020; Received in revised form 1 September 2020; Accepted 4 September 2020
Available online 11 September 2020

ordered lamellar bone (Currey, 2006; Kerschnitzki et al., 2011a; Shapiro, 2008). During the final remodeling phase, the woven bone is gradually replaced by lamellar bone leading to the re-establishment of the form and function of the pre-fractured bone structure (Schmidt-Bleek et al., 2014). The spatial–temporal succession of tissue formation, replacement and remodeling during secondary healing are similar in most mammals and give rise to intricate tissue patterns, in which different tissues are in contact with each other. An important question concerns the nature of the interfaces between tissues, specifically how continuous or discontinuous the transitions are from one tissue to the other.

The question of (dis)continuity relates not only to tissue composition and organization, but also to possible transport pathways between tissues housing the osteocyte lacuno-canalicular network (LCN). This network is formed when osteoblasts are incorporated into the bone matrix and differentiate into osteocytes. It remains unclear whether the osteoblast to osteocyte transition is a passive process whereby osteoblasts become entombed in osteoid (Franz-Odendaal et al., 2006; Nefussi et al., 1991) or is an active process involving proteolytic degradation of the extracellular matrix (ECM) to form the LCN (Holmbeck et al., 2005; Zhao et al., 2000). The osteocytes form a cellular network with the cell bodies located in cavities, known as lacunae, and their cell processes reside in narrow canals, the canaliculi. The LCN serves both transport and signaling functions, yet evidence is increasing that osteocytes also make use of the large surface of the LCN to resorb and deposit mineral, thereby contributing to mineral homeostasis (Roschger et al., 2019). This concept of osteocytic osteolysis is under debate since several decades and indications are found that this process may have significant physiological and pathophysiological importance (Tsourdi et al., 2018), but there are also several arguments against it (Boyde, 1980). A recent study on turkey leg tendons revealed interrelationships between an extensive tendon lacuno-canalicular network, the extracellular matrix and mineral deposits, suggesting a mechanism where the lacuno-canalicular system facilitates the transport of mineral ions and possibly mineralization precursors (Zou et al., 2020).

Recently research on the LCN gained momentum due to new imaging techniques, making it possible to visualize the three-dimensional architecture of the network in substantial bone volumes (Weinkamer et al., 2019). X-ray phase nano-tomography (Bach-Gansmo et al., 2016; Hesse et al., 2015) and ptychographic X-ray computed tomography (PXCT) (Dierolf et al., 2010) use the intensive and coherent X-rays of synchrotrons to image the LCN with a voxel side length up to 40–50 nm. An even higher resolution -accompanied with a smaller imaging volume- is possible with focused ion beam/scanning electron microscopy (FIB/SEM) (Schneider et al., 2011). A very efficient approach to image large regions of the LCN is to combine rhodamine staining with confocal laser scanning microscopy (Kerschnitzki et al., 2011b). With this approach it was shown that the structure of the LCN depends on the surrounding bone type (Kerschnitzki et al., 2013, 2011b); lamellar bone contains well aligned canaliculi and flattened lacunae, while in woven bone lacunae have a rounder shape and the fewer canaliculi are more irregularly arranged (Hernandez et al., 2004; Kerschnitzki et al., 2013). For human osteonal bone it was reported that lateral canaliculi, i.e. canaliculi not oriented towards the Haversian canal, are co-aligned with the preferred fiber orientation of the collagen matrix (Repp et al., 2017). Although numerous histological examinations have been applied to the LCN within the bony callus (Han et al., 2018; Marsell and Einhorn, 2012), there is lack of studies focusing on its three-dimensional architecture.

Structural characterization of the different tissue types in the healing bone is essential for providing insights into how these tissues are formed as well as how they influence each other. An important contribution to the stiffening of the callus relates to the mineralization of tissues. X-ray scattering techniques make it possible to determine the thickness of the nanometer-sized carbonated hydroxyapatite particles in bone (Fratzl et al., 2004). With backscattered electron microscopy the local mineral content of the bone can be quantified (Roschger et al., 2008). In previous healing studies on small animal models it was shown that the osteotomized region exhibits intricate patterns of various nonmineralized tissue types (cartilage, bone marrow, fibrous connective tissue) and mineralized ones (cortical tissue, callus-woven, callus-lamellar, calcified cartilage) and that the mineralized tissues do not only differ in collagen fibril organization, but also that the mineral particle density, orientation and shape contributes to the reduced mechanical competence of woven as compared to lamellar bone (Hoerth et al., 2018). During bone healing, an increasing degree of collagen fibril and mineral particle alignment was observed in the callus region coupled with increasing mineral platelet sizes (Hoerth et al., 2014; Manjubala et al., 2009). The properties of both, the collagen matrix and the mineral particles, play an important role in the mechanical characteristics of bone (Fratzl et al., 2004; Fratzl and Weinkamer, 2007). This may explain why many organisms replace less organized mineralized tissues with higher organized tissues.

In the current work a murine femoral osteotomy model was used to pursue the following two aims: (i) to identify and image structural characteristics of the main types of tissue (cortical tissue, bony callus, calcified cartilage) around the osteotomy site and (ii) to elucidate potential spatial correlations between the lacuno-canalicular network (LCN) and the mineral nanostructure of the surrounding extracellular matrix (ECM) to learn more about the role of osteocytes in mineralization processes. We map structural changes depending on the position of the tissue, i.e. in close vicinity to other tissues or further away, with an emphasis on the interfaces between cortical and callus tissue. Our strategy is to use a combination of different techniques to obtain three-dimensional and two-dimensional maps of material characteristics: Synchrotron-based micro-computed tomography (μCT) to characterize osteocyte lacunae, confocal laser scanning microscopy (CLSM) to image the three-dimensional LCN architecture, high-resolution synchrotron scanning small and wide angle X-ray scattering (SAXS/WAXS) to determine the mineral nanostructure and quantitative backscattered electron imaging (qBEI) to analyze the calcium content of the mineralized matrix.

2. Materials and methods

2.1. Samples and sample preparation

Three female, 26 week old -skeletally mature- C57BL/6J mice (Jackson Laboratory, Bar Harbor, Maine, USA) underwent an osteotomy at the mid-diaphysis of the left femur. An antibiotic (Clindamycin, dose of 45 mg/kg) and analgesic (Buprenorphine slow release, dose of 1 mg/kg) were administered with a subcutaneous injection prior to surgery. Mice were anesthetized with a 2% isoflurane oxygen mixture, which was administered throughout the surgery via a nose cone. The left femur was shaved on the lateral side from the knee to the hip. An approximately 1.5 cm long incision through the skin was made with a scalpel and the fascia lata was dissected, followed by separation of the M. vastus lateralis and M. biceps femoris to expose the femur. Four holes were drilled into the femur and an external unilateral fixator was mounted in the cranio-lateral direction onto the femur with four Mini-Schanz screws (pins) (0.45 mm, RISystem, Davos, Switzerland). A 0.5 mm osteotomy was created between the inner screws using a 0.44 mm Gigli wire saw (RISystem AG, Davos, Switzerland). Then, 2–3 topical drops of a solution containing Lidocaine 1% and Bupivacaine 0.25% were applied to the surgical site and the wound was closed by suturing the muscle fascia and then the skin. For pain management the animals received Tramadol hypochloride (25 mg/l) ad libitum through drinking water up to the third day after surgery. The three osteotomized mice (MF1-3) were sacrificed 21 days post-osteotomy as well as one not operated littermate serving as control. After dissection of the femora, the external fixator was removed and the bones were put immediately in 70% ethanol. The animal

experiments were carried out according to the policies and procedures approved by the local legal research animal welfare representative (Shriners FACC 2016-7821).

For sample preparation, the bones were dehydrated by immersion in ascending grades of ethanol (70%, 80%, 90% and 100%). Thereafter, samples were stained overnight with a solution of Rhodamine6G (Rh6G, Sigma Aldrich GmbH, Taufkirchen, Germany) and pure ethanol. Rhodamine stains non-mineralized tissue, osteoid and the small size of the rhodamine molecule ensure deep penetration of the stain reaching all the porosities in the mineralized tissue, including the LCN. To stabilize the samples for cutting and polishing, they were embedded in Polymethylmethacrylate (PMMA). The obtained femur-PMMA blocks were cut into two halves. One half of the blocks were cut into slices along their longitudinal axis with a microtome (Leica SM2500S and Leica VMH 400 knife, Nussloch, Germany) and polished (PM5 Logitech, Glasgow, UK) to a final thickness of approximately 5 µm. Some slices were used for histological staining (Giemsa and Masson-Goldner), the slice closest to mid-section of each sample, i.e. the remaining block, was mounted on a silicon nitride X-ray-transparent window (1 µm thick nitride window with a 500 µm thick silicon frame, Norcada Inc., Edmonton, Canada) and was used for SAXS and WAXS experiments. Following grinding and polishing, the other halves of the blocks were first imaged by CLSM and then by qBEI. For the qBEI experiments, the block surfaces were coated with a thin carbon layer by vacuum evaporation (Ager Scientific, SEM carbon coater, Essex, UK) to prevent charging using scanning electron microscopy (SEM).

2.2. Material properties

Small- and wide-angle X-ray scattering (SAXS/WAXS) measurements were performed at the microfocus beamline (ID13) at the European Synchrotron Radiation Facility (ESRF, Grenoble, France) for all four samples (three with and one without surgery). In this manuscript, we provide extensive details about the results of MF1, i.e. maps, mean values and standard deviation values. During the scanning experiments SAXS and WAXS were measured simultaneously. Using an x-y-z-stage the samples were moved relative to the beam with a step size of 2 µm, defining the coordinate system for further evaluations. With a nominal beam size of approximately 2 µm the samples were exposed to X-rays of the wavelength 0.95 Å (photon energy of 13 keV) for 85 ms. The SAXS/WAXS patterns were recorded with an Eiger X 4 M detector (Dectris AG, Baden Dättwil, Switzerland) with an image size of 2070 × 2167 pixels and a pixel size of 75 × 75 µm^2. The q-range covered 0.1–3 nm^{-1} (SAXS) and 15–20 nm^{-1} (WAXS). The scan area per sample was several hundred micrometers in size, resulting in a total of 557,570 measured scattering patterns. The SAXS and WAXS data were evaluated with the DPDAK software tool (Benecke et al., 2014), which uses integration and calibration algorithms from the pyFAI package (Kieffer and Wright, 2013). The detected intensity (I_{sample}) was corrected by subtracting the background intensity. Using the motor position of the stage, distribution maps of the resulting data were created. The software Fiji (Schindelin et al., 2012) was used to read out the pixel coordinates (x-y-plane) of regions of interest.

The mineral particles (hydroxyapatite) of bone usually have the shape of thin platelets (Fratzl et al., 2004). The average thickness of these platelets is estimated by the T parameter $T = (4\Phi (1- \Phi))/\sigma$, where Φ describes the total volume and σ describes the total surface area of all particles per unit volume. Thus, the relation of Φ and σ indicates the volume-to-surface ratio of the particles (Fratzl, 1994). To filter and distinguish points from either mineralized matrix or unmineralized regions, we added a threshold of the total scattering intensity, assuming a corresponding threshold of material amount in the corresponding volume. Moreover, the T parameter evaluation was limited by Porods law (Porod, 1951), i.e. the T parameter was evaluated for points, where the scattering intensity decreased with q^{-4}. The T parameter determination assumes a mineral volume fraction of 50% (Pabisch et al., 2013), but especially in callus regions there might be deviations from this assumption. In principle, the mineral volume fraction could be measured independently by quantitative backscattered electron imaging to apply corrections for the T parameter and calculate a corrected mineral particle size parameter. However, the mineralization levels in the callus region are mostly lower compared to the cortical tissue regions, leading to a slight overestimation of the mineral particle size.

The degree of orientation defined as ρ parameter was calculated by the azimuthal SAXS intensity profile $I(\chi)$. A ρ parameter of 1 corresponds to a uniform orientation of mineral particles, while a value of $\rho = 0$ describes a completely random distribution of particle orientations (Rinnerthaler et al., 1999). The ρ parameter describes the projected degree of orientation within the plane perpendicular to the incident X-ray beam and is not a full measure of a three-dimensional degree of orientation of the mineral particles. The crystal length L along the c-axis was determined from the full width at the half maximum of the (0 0 2) peak intensity in the WAXS signal using Scherrer's equation $L = (k\cdot\lambda)/(B \cdot \cos(\theta))$, with the wavelength λ, the Bragg angle of the peak θ, the Scherrer constant $k = 0.9$ and the full width at the half maximum B of the peak in radians. Not only the finite size of the crystals causes this peak broadening, but also other effects, especially the instrumental broadening. However, a Voigt function, which is a convolution of Cauchy and Gaussian functions, describes the pure diffraction line profile of biological apatite (Danilchenko et al., 2002). The position of the 002 peak refers to the d-spacing in crystallographic 002 direction, i.e. the inter-atomic space, which is used to calculate the c lattice constant (Handschin and Stern, 1995).

2.3. Imaging techniques

The bone mineralization density distribution (BMDD) (i.e., a frequency distribution of bone mineral content) was determined with a scanning electron microscope (Supra 40, Zeiss, Oberkochen, Germany) equipped with a four-quadrant semiconductor backscatter electron (BE) detector for all samples. The scanning electron microscope (SEM) was used with the following setup: 10 mm sample-detector-distance, 130x nominal magnification, 20 kV acceleration voltage and a probe current between 270 and 320 pA. Each pixel (size: 0.88 × 0.88 µm^2) has a certain gray level (256 gey level steps), which represents a corresponding mineral content. The calibration of the BE signal was performed according to the standard procedure described by Roschger et al. (1998) with calibration standards Aluminum (grey value 225 ± 1) and Carbon (grey value: 25 ± 1). Consequently, the grey value of pure hydroxyapatite (HA) is 255, the grey value for 0% HAP is 25. For each sample, we calculated the BMDD and the reported mean values for the depicted bone tissue separately.

To determine the architecture of the LCN from the femur-PMMA blocks, a Leica TCS SP8 (Leica Microsystems GmbH, Wetzlar, Germany) equipped with a 40x oil immersion microscope objective (numerical aperture of 1.3) was used. An image size of 1024 × 1024 px (pixel size 284 × 284 nm^2) was chosen. An argon laser (max. 65 mW) with an excitation wavelength of 514 nm serves for point illumination, while the emission was measured at a range from 550 nm to 650 nm. Image stacks were taken with a spatial z-resolution of 300 nm for all samples.

To visualize the LCN architecture within its mineralized surroundings, qBEI images and CLSM z-projections were overlaid onto each other. For this purpose the z-stacks of approximately 2 µm (similar information depth like penetration depths of electrons in qBEI measurements (Goldstein et al., 2018)) were projected from 3D in 2D with ImageJ v.1.51n (Schneider et al., 2012) using the standard deviation (STD) projection type. A fixed threshold with the graphics software Adobe Photoshop (CS5 v.12.0.4) was used to extract the LCN from the z-projections for visualization. As osteocyte lacunae at the block surface are clearly visible in both datasets, these features allowed accurate image registration.

We performed synchrotron-based phase contrast enhanced micro-computed tomography (CT) at the beamline ID19 at the ESRF on two selected samples. The phase contrast was used to enhance the visibility of edges of lacunae and pores providing more accurate results for pore segmentation. The effective pixel size on the detector was 650 × 650 nm^2, and the detector field of view was 1.4 × 1.4 mm^2. A total of 4200 up to 4600 projection images were recorded over a rotation of 360°, with a counting time of 80 ms resulting in a scan time of 10.5 min for each sample. For the subsequent image analysis a sample-to-detector distance of 25 mm was used to achieve best contrast performance for the subsequent image analysis.

To determine lacunae shape, size and distribution in cortical and callus regions a multi-step image analysis was performed. First, a non-local means filter was used for noise reduction in the image. Then a histogram-based global thresholding method was used to segment the pre-processed 3D data, where the minimum in the grey-level distribution was chosen to separate bone from pore space (Vorauer et al., 2020). In the binarized image, the morphological operations of dilation and erosion together with the same input parameters were applied to correct segmentation errors, e.g. over- and under-segmented lacunae. The application of both dilation and erosion improved the segmentation. To be analyzed as lacuna, a pore had to be larger than 50 μm^3, which is larger than the reported volume of canalicular junctions (Wittig et al., 2019) and smaller than reported volumes of lacunae, i.e. between 200 and 600 μm^3 (Heveran et al., 2018). Larger porous structures such as blood vessels were excluded by applying an upper threshold of 1000 μm^3.

The two volumes of interest (VOIs) of the μCT measurements (1723 × 1560 × 1300 μm^3 and 739 × 747 × 65 μm^3, respectively, see Fig. 1a and b) were evaluated in two different ways. The first evaluation approach focused on the determination of reference values for the cortical region and the bony callus, respectively. Consequently, 70 cubic subvolumes (65 × 65 × 65 μm^3) were selected from the larger VOI (Fig. 1a) within both, the cortical region and the bony callus. The size of the subvolumes were chosen with respect to a compromise: large enough to provide enough statistics and, therefore, to obtain a meaningful value for the lacunar density, and small enough to be able to study a spatial heterogeneity of the lacunar density. Concerning the positioning of the subvolumes, we decided against a positioning on a regular grid not only to avoid the bone surface, but also due to heterogeneous nature of rodent long bones. While the 70 cubic subvolumes were distributed over the whole imaged volume to cover a representative volume, their locations were chosen to avoid interface and surface regions, and to place them only within the woven as well as more lamellar regions of cortical bone. The same applies to the callus (Fig. S1). In addition, the cubes were selected in different depths for the different regions (cortical region and bony callus) to allow for a representative statistical quantification in image analyses. We validated the accuracy of the segmentation by checking slice by slice for selected cubes of both cortical region and bony callus regions. Using a second evaluation approach we performed a detailed analysis of lacunar properties at the interface between the cortical and callus region (Fig. 1b). For this analysis the smaller VOI was used and the interface between cortical and callus regions was defined manually based on clear differences in the grey values between the two tissues followed by a spline interpolation. The distance between lacuna and interface is defined as the shortest distance of the center of mass of the lacuna and the interface. The segmented pores on the right (callus) and left (cortical region) side of the defined interface are shown in blue in Fig. 1c.

The lacunar properties were analyzed according to the framework of former studies (Dong et al., 2014; Mader et al., 2013). Lacunar volume (Lc.V) is simply calculated based on the number of voxels in the pore. For the lacunar density, Lc.N/TV, only lacunae with their center of mass within the cubic subvolume of evaluation were considered. The morphology of the lacunae was characterized using the inertia matrices of each lacuna with reference to its center of mass. With the eigenvalues of this matrix $\lambda_{1\text{-}3}$ with $\lambda_1 < \lambda_2 < \lambda_3$, the lacunar stretch is defined as Lc. St = $(\lambda_3 - \lambda_1)/\lambda_3$. Its extrema indicate either a perfect sphere (Lc.St = 0) or an infinitely stretched object (Lc.St. = 1). If Lc.St ≠ 0, the lacunar oblateness Lc. Ob = $2\frac{\lambda_2 - \lambda_3}{\lambda_1 - \lambda_3} - 1$ takes also the third eigenvalue into account and characterizes whether the shape is more prolate-like, when the first two eigenvalues are close to each other (Lc.Ob ≈ −1) or oblate, when λ_2 is closer to λ_3 than to λ_1 (Lc.Ob ≈ 1) (Mader et al., 2013). We used Python 3.6 for image analysis and Avizo® (version 2019.1) to visualize the obtained results. Welch's *t*-test determines the effects of the tissue type.

3. Results

3.1. Microstructure and mineralization density distribution

Quantitative backscattered electron imaging (qBEI) (Fig. 2) provides information on microstructure and mineral content of the murine femora and gives an overview of the healing state of the bone. Based on the morphology and grey-levels it was possible to differentiate (i) the dense cortical bone (Fig. 2, white arrow heads) with a high mineral content and uniform appearance, (ii) the rather loose and lower mineralized bony callus bone (red arrow heads) and (iii) the calcified cartilage (blue arrow heads) with its characteristic round pores. This classification of tissues was confirmed by histology as shown in the supplementary information (Fig. S2).

The mice underwent the same osteotomy surgery and were stabilized using external fixators with the same stiffness. Although all show the formation of mineralized callus tissue, the different animals exhibit substantially different healing patterns (Fig. 2). The fracture ends of mouse femur 1 (MF1) are aligned almost along the pre-osteotomized position and show periosteal bony callus bridging as well as an endosteal mineralized callus. The upper and lower fracture ends of MF2 are not well aligned and the healing progress is limited with mineralized callus tissue being formed only locally. MF1 and MF2 show a vesicular structure between the adjacent fracture ends which is identified by histological staining as cartilaginous tissue (see supplementary information).

The Ca content of the cortical tissue is high ($Ca_{mean} \approx 27.5\ wt\%$ and $Ca_{mean,Control} \approx 27.1\ wt\%$ in the control sample) and it is homogenously mineralized as reflected by a small width of the bone mineralization density distribution (BMDD) $Ca_{width,Cortex} \approx 3\ wt\%$ and $Ca_{width,Control} \approx 3.1\ wt\%$in the control sample). Only near the interface with the bony callus, the Ca content of the cortical tissue slightly decreases. Compared to the cortical tissue, the bony callus tissue shows a substantially lower Ca content, i.e. Ca_{mean}ranges from 22.16 to 23.39 wt % Ca. Furthermore, with $Ca_{width} \approx 5.6\ wt\%$ the BMDDs are broader than those of the cortices reflecting a more inhomogeneous mineral content. However, qBEI shows cortex fragments (CF) resulting from the osteotomy process (see also Fig. 3 MF1 [i]) and highly mineralized islands (black asterisks in Fig. 3, MF1 [ii]) across the callus tissue without any lacunae.

MF1 shows calcified cartilage at the fracture ends (see Fig. 2 and Fig. S2), while the calcified cartilage of MF2 is located in the central callus tissue within the opposing fracture ends. In both cases, the cartilage shows a strongly heterogeneous Ca content covering the full range from very low calcium content up to the highest detected Ca values (see Fig. 2).

3.2. Lacuno-canalicular network and its mineralized surroundings

The plots in Fig. 3 show a superimposition of qBEI images with the image of the rhodamine-stained LCN on top for selected regions. MF1 [i] covers an extended region within the osteotomy gap. At the cartilage area next to the cortices, regions with a low Ca content can be found, which are fully rhodamine-stained and, therefore, appear red. In

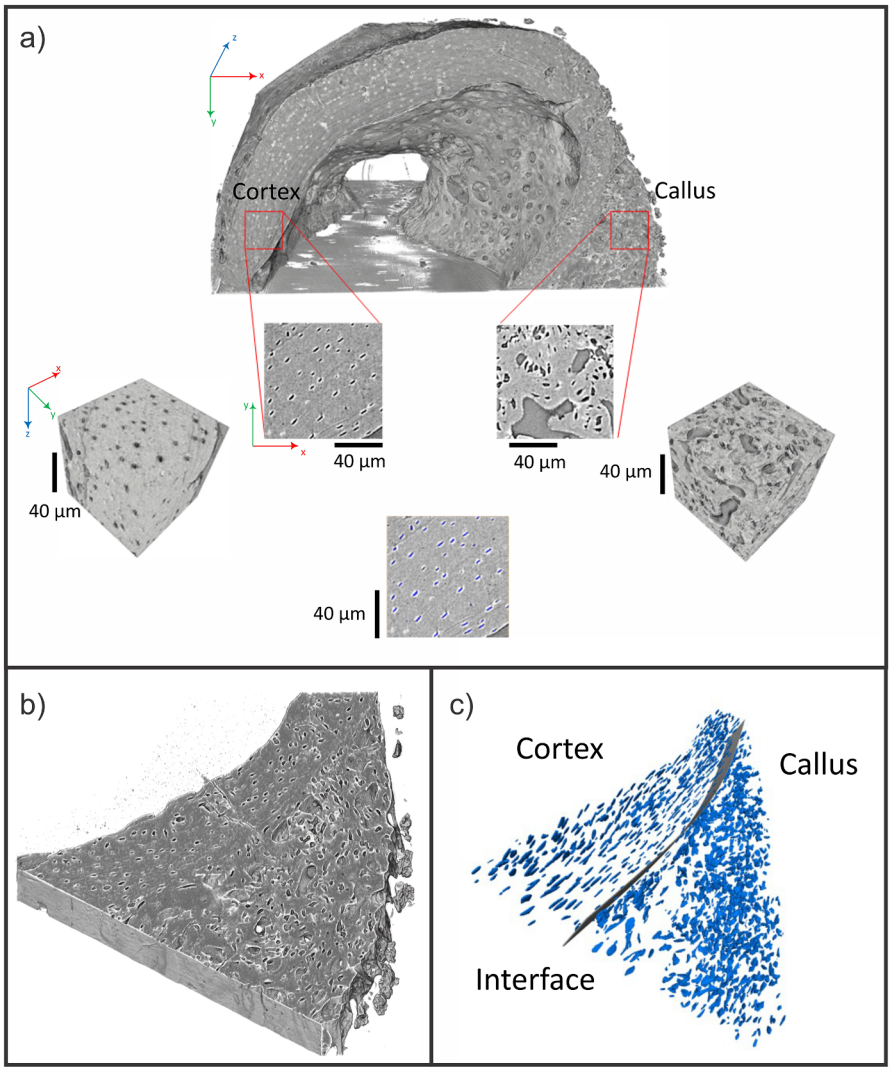

Fig. 1. Synchrotron-based micro-computed tomography measurements. 3D reconstruction of a portion of callus and cortical bone (a). The segmented lacunae were analyzed within cubes with a side length of 65 µm. To analyze the behavior at the interface, a layer with the contrasting bone types, cortical tissue and callus, was chosen. The VOI of 739 * 747 * 65 μm^3 is shown as a phase contrast image (b) and segmented volume with a defined interface between the bony callus and cortical tissue (c).

contrast, MF1 [i] shows also regions without staining, which are most likely cortex fragments (labeled by CF in Fig. 3), that became detached from the cortex during the osteotomy process. MF1 [ii] and MF3 [i] display both an endosteal callus region. Gross observation shows that these areas show highly aligned canaliculi, running radial from the vascular channels (labeled by V) and from the lacunae (yellow asterisks), respectively, connecting other lacunae in their vicinity. Besides this, the LCN seems to be randomly arranged. Again, regions without staining can be identified, which have a particular high Ca content (labeled by black asterisks). Also the surrounding of these mineralized islands exhibits negligible staining.

In sample MF3 [i] it is clearly seen, that the architecture of the LCN in the cortical region differs from the one in the callus. The lacunae of the cortical region exhibit a more elongated shape and their longest axis seem to be well aligned with the longitudinal axis of the femur. In contrast, lacunae of the callus exhibit a more roundish shape. The callus also features more lacunae, but fewer connecting canaliculi. The canaliculi within the callus run without a preferred orientation, while the canaliculi in the cortical region are preferentially oriented perpendicular to the longitudinal axis of the femur.

In the transition zones between the cortical and callus region (as can be seen in Fig. 3 MF3 [i]) most of the canaliculi from the cortical region do not proceed to the callus region. The appearance of canaliculi is markedly different in cortical and callus regions with canaliculi appear thinner in cortical regions. At the interface between cortical and callus regions vascular channels are located and areas of high mineral content without any lacunae or canaliculi interrupt the continuity of the LCN.

3.3. Osteocyte lacunae number, volume and shape

Evaluation of the cubic subVOI positioned either in the cortical region or in the bony callus of MF1 (Fig. 1; Fig. S1) showed that the lacunar density (Lc.N/TV) as well as the mean lacunar volume ($< Lc.V >$) were both significantly higher in the callus ($\approx (100 \pm 19) * 10^3\ mm^{-3}$ and $290 \pm 177\ \mu m^3$) than in the cortical region ($\approx (73 \pm 15) * 10^3\ mm^{-3}$ and $151 \pm 55\ \mu m^3$) (see Fig. 4 and Table 1). Fig. 5 shows the obtained size and shape information of all the lacunae using the evaluation approach based on cubic subvolumes within the cortical region and the callus (Fig. 5a, b, e, f). In the cortical region two lacunar properties show conspicuously low variability: Lc.V (Fig. 5a) and the lacunar stretch (Fig. 5e) ($< Lc.St >_{cortex} = 0.80 \pm 0.06$). The negative values for the oblateness indicate

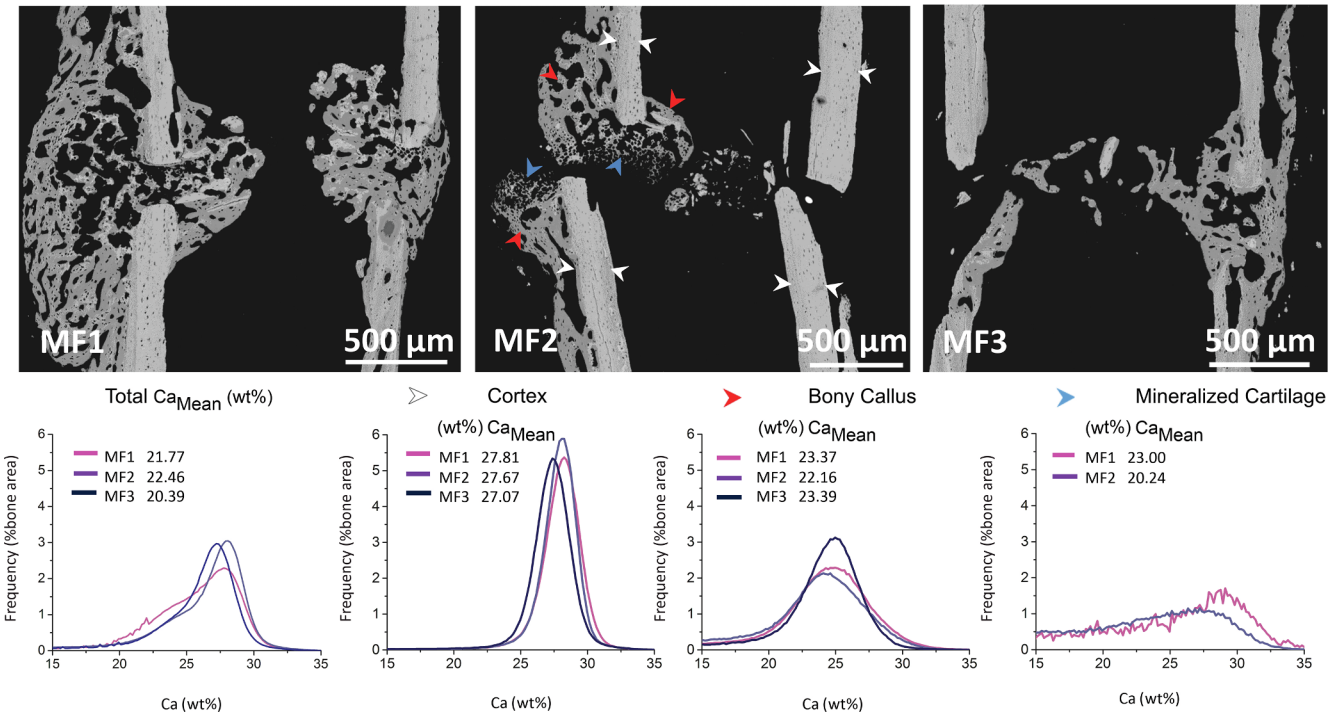

Fig. 2. Quantitative backscattered electron imaging (qBEI) of three samples MF1, MF2 and MF3 showing the healing status of each sample 21 days post-osteotomy. Grey levels in the images correspond to the local Ca content with high regions of high Ca content being depicted bright. All three samples show callus formation between the proximal and distal osteotomy fracture ends in the cutting plane. Additional regions of calcified cartilage can be found only in MF1 and 2. The arrow heads mark the three mineralized tissue types of interests: (white) cortical bone, (red) bony callus bone and (blue) calcified cartilage. Differentiation between tissue types were based on morphological features (e.g., osteocyte lacunae), the local Ca content (grey level), and were confirmed by histological sections (see Fig. S2). Below are shown the bone mineral density distributions (BMDDs), i.e. the frequency distribution for the Ca content, for the whole image and the three mineralized tissues separately. (For interpretation of the references to color in this figure legend, the reader is referred to the web version of this article.)

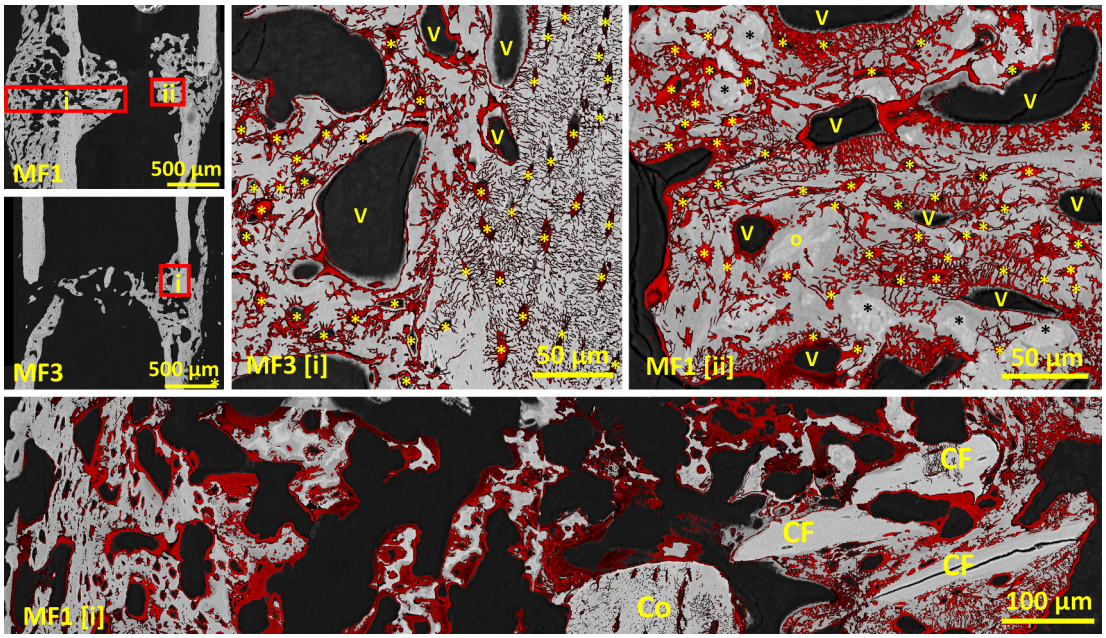

Fig. 3. Overlay of quantitative backscattered electron images (qBEI) and confocal laser scanning microscopy (CLSM) z-projections with an information depth of 2 µm for both methods. The qBEI images depicts the Ca content of the cortical and callus region in grey scale. Rhodamine6G stains all inner surfaces: osteocyte lacunae (yellow asterisks) and soft tissue appear with red stained areas or lines, vascular channels (V) are typically surrounded by a red layer. The left qBEI images serve as orientation for the following regions of interest. MF3 [i] shows an interface between the cortical and endosteal callus region. MF1 [i] is an overview of the callus region from sample MF1. MF1 shows different types of mineralized tissue, cortical region (Co), bony callus, calcified cartilage, but also cortex fragments (CF) from the osteotomy process. MF1 [ii] displays a region of the callus structure surrounding islands of high mineral content (black asterisks) and vascular channels. (For interpretation of the references to color in this figure legend, the reader is referred to the web version of this article.)

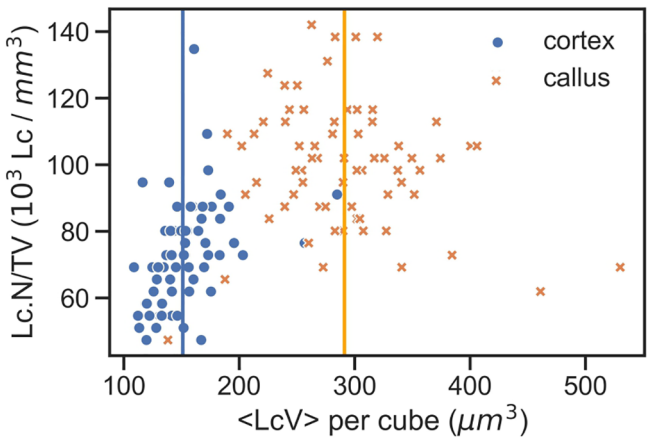

Fig. 4. Lacunae number density vs. average lacunar volume from μCT data using the evaluation approach with cubic subvolumes. Analysis of individual subvolumes distributed throughout the imaged bone volume (cortical and callus region). The orange crosses correspond to average lacunar properties from cubes in the callus and the blue dots from cubes in the cortical region, respectively. The solid lines in blue and orange indicate the mean value of the respective bone type. (For interpretation of the references to color in this figure legend, the reader is referred to the web version of this article.)

a prolate shape of the lacunae ($< Lc.Ob_{Cortex} >$ = -0.16 ± 0.37). In contrast, lacunae in the callus show more diverse sizes and shapes. In the callus the lacunae are more roundish with lower values of Lc.St compared to the cortical region ($< Lc.St_{Callus} >$ = 0.72 ± 0.11) (Fig. 5f compared to 5e). Lc.Ob is smaller ($< Lc.Ob >_{callus}$ = -0.25 ± 0.40) and, therefore, the lacunae are more prolate than in the cortical region (Fig. 5f).

Shifting now the focus towards the transition zone between callus and the cortical region, we observe that the cubic subvolumes in the cortical region in Fig. 4 with very large lacunae or very high lacunar density are located rather close to the interface within the callus region. Analysis of the transition zone between cortical and callus regions (VOI of Fig. 1b, c; see also Fig. S3 for information of how far the analyzed bone volume is located from the interface) and comparing the obtained results (Fig. 5c, d, g, h) to the results from within the callus and cortical region (Fig. 5a, b, e, f), we see clear differences that imply an influence of the two different tissues on each other. The analysis from the transition zone on the side of the cortical region shows an increase of the size of the lacunae (Table 1) and a broader distribution of the lacunar volume than within the cortical region (Fig. 5c compared to Fig. 5a). It is remarkable, that the distribution of both Lc.V and Lc.Ob in the cortical region and callus at the interface (Fig. 5c and d) are more similar to each other than within each cortical region and callus separately (Fig. 5a, b). This observation also holds true when comparing the shape characteristics of the lacunae: also here Fig. 5g) and h) resemble each other more than the corresponding plots Fig. 5e and f.

The lacunar properties near the interface revealed in more detail from plots of the lacunar volume and the lacunar oblateness as a function of the distance from the interface (Fig. 6). For the lacunar volume (Fig. 6a) there is a clear discontinuity at the interface. On the cortical side (left to the interface) the size of the lacunae is not only smaller, but the variability is clearly lower compared to the callus. Lacunae larger than 400 μm are almost exclusively found on the side of the interface, where the bony callus was formed. The average lacunar volume in our VOI close to the interface was determined to be 197 μm^3, which is larger than the corresponding reference value for the cortical region (151 μm^3) obtained by the approach based on cubic subvolumes. The average lacunar volume on the callus side (right to the interface) is higher (327 μm^3) than the corresponding reference value for the callus (290 μm^3). The situation is very different for the oblateness describing the shape of the lacunae (Fig. 6b). Here the transition between cortical and callus region is so smooth that it would be difficult to locate the interface without the information provided by the x-axis of the plot. However, the reference values for oblateness for the callus and the cortical region were already also very similar.

3.4. Ultrastructure of mineral particle parameters in healing bone

High resolution synchrotron SAXS and WAXS were used to elucidate the nanostructural mineral particle characteristics, namely thickness and length (T and L parameter) as well as the alignment of their orientation (ρ parameter) and the c lattice parameter in a position-resolved manner across the different tissue types. Comparing the resulting color maps (see Fig. 7) with the results of qBEI allows a distinction between the types of bone, which is reflected by different characteristics in the nanostructure. As shown in Fig. 7 for sample MF1, the cortical tissue exhibits long, thick mineral particles with a relatively high degree of orientation and high c lattice parameter ($< L_{Cortex} >$ = 24.36 ± 2.93nm, $< T_{Cortex} >$ = 2.86 ± 0.26nm, $< \rho_{Cortex} >$ = 0.5 and $< c_{Cortex} >$ = 6.822 ± 0.006 Å). The control sample showed the following average values: $< T_{Control} >$ = 2.60 ± 0.19 nm, $< \rho_{Control} >$ = 0.55 ± 0.13. In contrast, most of the bony callus bulk regions show a smaller degree of particle alignment with ($< \rho_{Callus} >$ = 0.37) and thinner mineral particles ($< T_{Callus} >$ ≈ 2.50 nm). The calcified cartilage shows thin and poorly oriented particles ($< T_{Cartilage} >$ ≈ 2.17 nm, $< \rho_{Cartilage} >$ ≈ 0.22). A positive correlation between mineral crystal length (L parameter) and crystal lattice spacing was found by evaluating the WAXS measurements (Fig. 8). The average length of the mineral crystals hardly differs between calcified cartilage ($< L_{Cartilage} >$ ≈ 18.60 nm) and callus $< L_{Callus} >$ ≈ 18.70 nm), but is higher in the cortical tissue ($< L_{Cortex} >$ ≈ 24.36 nm), while the thickness and the lattice constant increase from calcified cartilage ($< c_{Cartilage} >$ ≈ 6.815 Å) to callus ($< c_{Callus} >$ ≈ 6.821 Å) to the cortical region ($< c_{Cortex} >$ ≈ 6.844 Å).

The thickness of the particles decreases from the bulk region of the cortex towards the interface with the bony callus, as well as the ρ parameter (see Fig. 7). Most of the callus transition zones show a higher degree of orientation (ρ ≈ 0.5) compared to their bulk region. The

Table 1
Lacunar properties in cortex and callus. The mean and standard deviations of the average lacunar volume ($< Lc.V >$), the average lacunar stretch ($< Lc.St >$), the average lacunar oblateness ($< Lc.Ob >$) and the average lacunar density ($< Lc.N/TV >$) are reported. Entries that are significantly different ($p < 0.001$) are indicated with an asterisks (Welchs-tests for all), n.s. stands for not significant. A total of 4007 lacunae were analyzed, see materials and methods for further description.

	Within tissue			At the interface			Comparison of bone type within tissue and at the interface	
	Cortex	Callus		Cortex	Callus		Cortex	Callus
Lc.N(#)	1152	1544		496	815			
Lc.V (μm^3)	151 ± 55	290 ± 177	*	197 ± 93	327 ± 187	*	*	*
Lc.Ob	−0.16 ± 0.37	−0.25 ± 0.40	*	−0.22 ± 0.39	−0.26 ± 0.41	*	n.s.	n.s.
Lc.St	0.80 ± 0.06	0.72 ± 0.11	*	0.76 ± 0.09	0.71 ± 0.11	*	*	n.s.
Lc.N/TV (10^3 /mm^3)	73 ± 15	100 ± 19	*					

callus regions with lamellar-like organization contain relatively thin mineral particles (T < 2.4 nm) while the regions around the lacunae exhibit thick minerals (T greater than 2.9 nm) (see also Fig. S4). Additionally, the thickness of the mineral platelets in the calcified cartilage increases also towards its transition zone to the bony callus.

4. Discussion

In this work, we applied a multi-method approach to visualize the lacuno-canalicular network architecture and to quantify structural characteristics in different types of mineralized tissue present in healing bone and, in particular, at the transition zone between the cortical region and callus. We used a mouse osteotomy model, which provided a large variety of structural characteristics across tissue types (cortical tissue, bony callus, calcified cartilage) corresponding to different stages in endochondral and intramembranous bone formation processes. This approach resulted in a multi-scale characterization of these tissues. Thereby, we elucidated potential correlations between structural features of the LCN architecture and mineral characteristics in view of the underlying bone formation mechanisms. Characteristic key features of

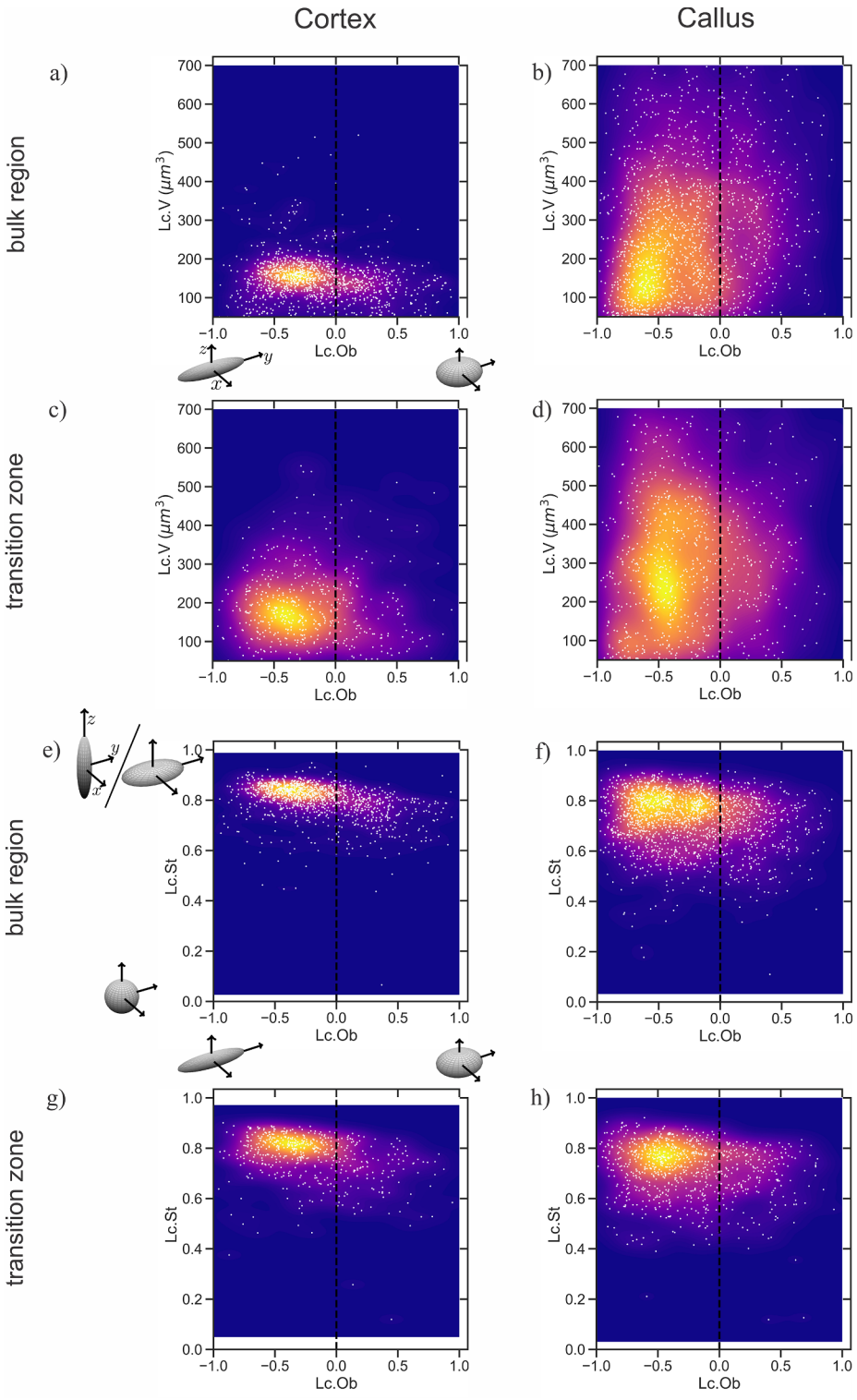

Fig. 5. Size (Lc.V) and shape (Lc.St, Lc.Ob) of lacunae measured by μCT within the cortical (a, e) and the callus region (b, f) in comparison with lacunar properties for the cortical and callus region (c, d, g, h) measured in a bone volume containing an interface between the two tissues (see Fig. 1b). Each white dot in the plots corresponds to one measured lacuna. For a better readability the scatter plots are underlaid with a density plot, where brighter colors imply higher density of measured points. Dashed line indicates Lc.Ob equals zero. Additionally, ellipsoids illustrate the stretched or roundish shape of lacunae (a, e). The oblateness of lacunae (Lc. Ob) as a function of lacunar volume (Lc.V) is plotted for the cortical region in (a) and for the callus in (b). The lacunar stretch (Lc. St) as a function of the oblateness is plotted in the cortical region in (e) and for the callus in (f). The corresponding plots for the transition zone between the cortical and callus region are shown in (c), (d) and (g), (h), respectively.

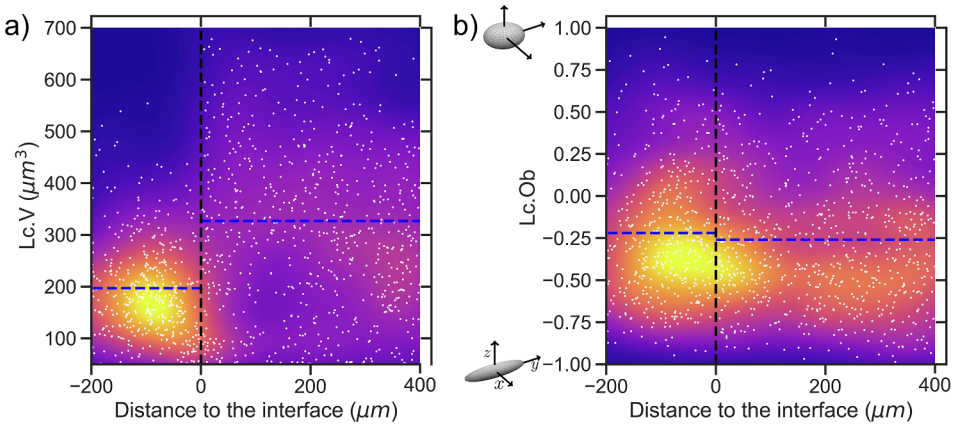

Fig. 6. Lacunar volume (a) and oblateness of lacunae (b) as a function of their distance to the interface between the cortical region and callus. Each white dot corresponds to one measured lacuna. The location of the interface is denoted by a black dashed line. Negative distances in the plots corresponds to the cortical region, positive distances to the callus. The blue dashed lines correspond to the reference values for Lc.V and Lc.Ob as obtained from an evaluation approach with cubic subvolumes located completely either in the cortical region or the callus. The oblate/prolate ellipsoids in (b) reflect the shape of lacunae at the particular part of the axis. (For interpretation of the references to color in this figure legend, the reader is referred to the web version of this article.)

the tissue types are summarized in Table S1.

Cortical bone regions exhibited typical characteristics as found in earlier studies for murine bone, i.e. an intracortical band with a rather low degree of organization surrounded by material with a higher degree of organization (Ip et al., 2016; Shapiro, 2008) being represented by the organization of the LCN as well as the mineral particle orientation (Kerschnitzki et al., 2011b). The cortical region generally shows higher values for mineral particle thickness and degree of orientation than the callus region (Hoerth et al., 2018). As secondary remodeling usually does not occur in rodents, the intracortical band – including cartilage islands and woven bone – presumably was formed during bone development and remains unremodeled in the adult mouse (Bach-Gansmo et al., 2013; Burr and Allen, p. 92/93, 2019). Similar findings are reported for the cortex of rats exhibiting a lower degree of matrix organization than lamellar bone (Shipov et al., 2013). In contrast to the observations of Bach-Gansmo et al. in rats, we could not observe any significant differences in lacunar properties between the inner and outer band (Bach-Gansmo et al., 2015). In the cortical region, the average lacunar density (Lc.N/TV ≈ 73 * 10^3 mm^{-3}) appears higher or in the same range as reported previously on bones in rodents, while the average lacunar volume (Lc.V ≈ 151 μm^3) is comparably lower (Schneider et al., 2007; Voide et al., 2011) or in a similar range (Tiede-Lewis et al., 2017).

The bony callus contains woven regions enveloped by lamellar ones,

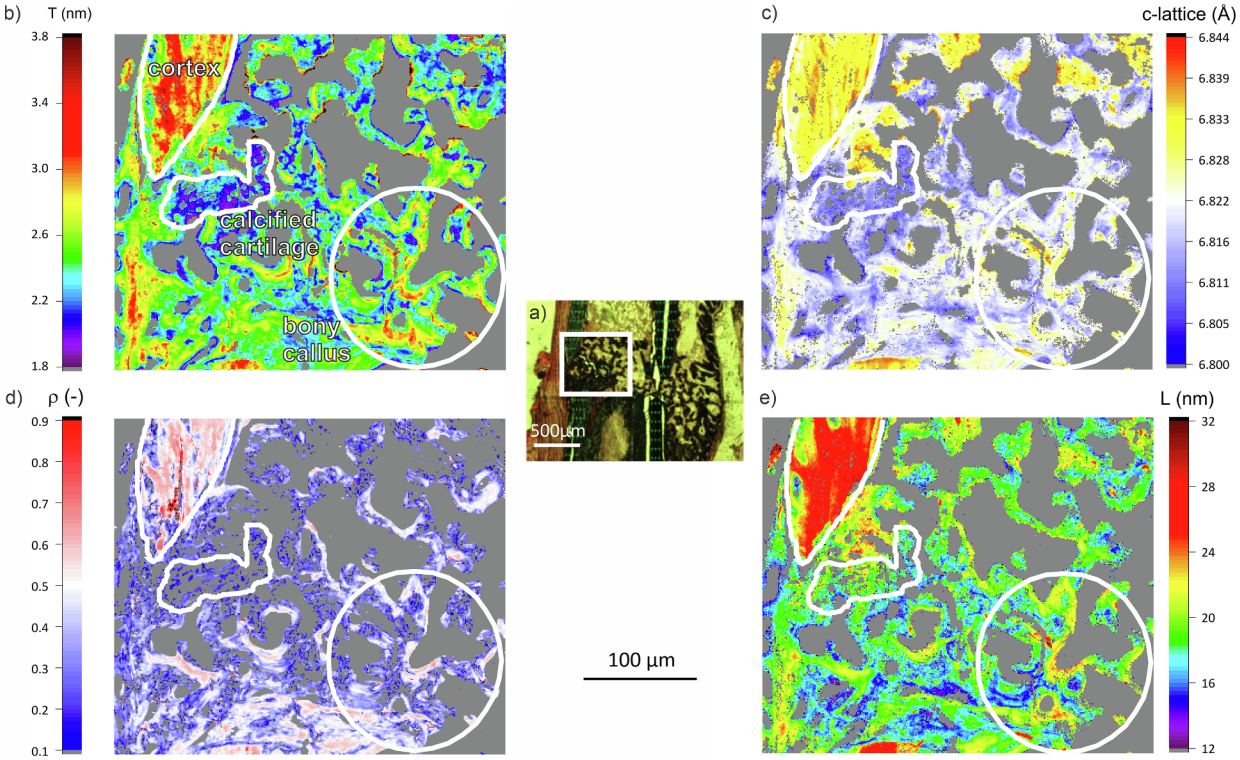

Fig. 7. Results from synchrotron small and wide angle X-ray scattering (SAXS/WAXS). Mineral particle thickness (T), orientation (ρ), crystal length (L) and lattice spacing (c lattice parameter) are represented by color maps of MF1. The white square in the light microscopy image in (a) marks the location of the region, which includes periosteal callus tissue, calcified cartilage tissue and osteotomized cortex. All maps originate from the same combined SAXS and WAXS measurement. For every measurement point the mean mineral particle thickness (T parameter) is shown color-coded in (b). The degree of orientation (ρ parameter) is evaluated in (d). The right side (c and e) shows WAXS results, the c lattice parameter (c) and the length L of the crystals (e). The gray colored data points in the color maps represent the filtered measurement spots, which did not contain enough mineral to give a sufficient X-ray scattering signal. Cortical bone can be found in the upper left corner of each map and is highlighted by a white line. The white line below the cortical region surrounds the region of calcified cartilage, while the white circle visualizes a region of the callus including different features such as woven as well as lamellar bone.

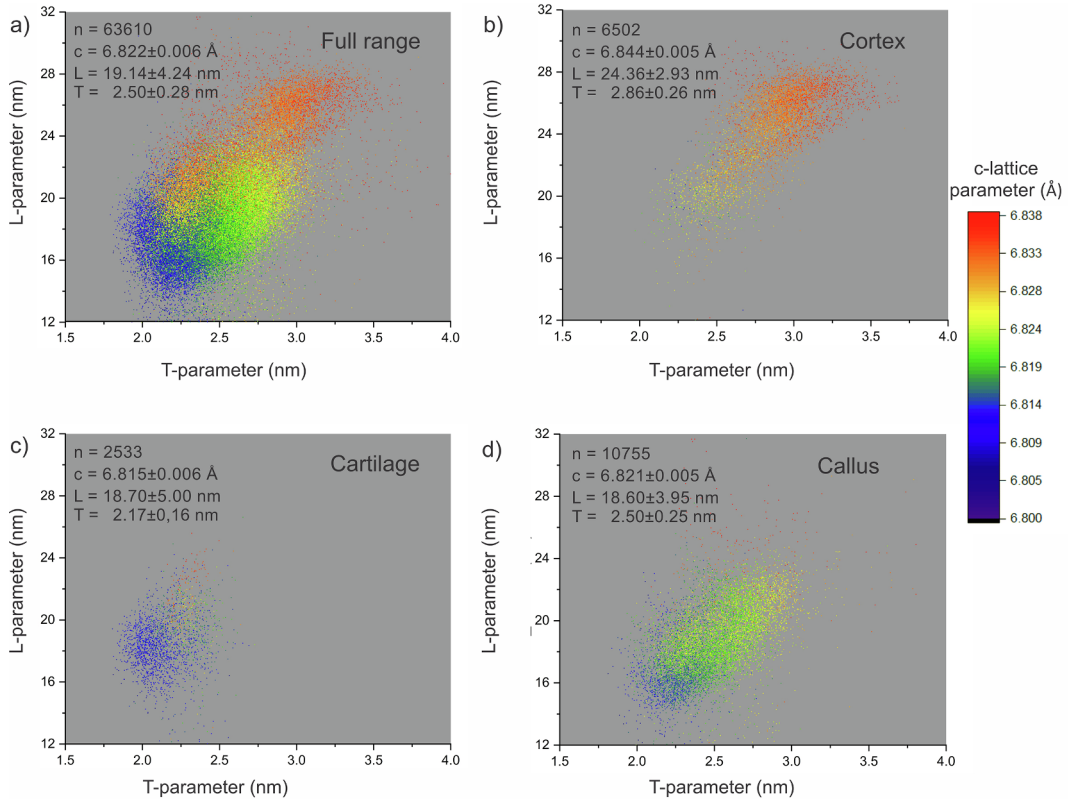

Fig. 8. Mineral particle characteristics (L: crystal length; c lattice parameter: crystal lattice spacing; T: particle thickness) as evaluated by wide and small angle X-ray scattering of MF1 of the corresponding regions in Fig. 7 (the whole region (a), cortical tissue (b), calcified cartilage (c), bony callus (d)). Based on crystal lengths and lattice spacing the different regions can clearly be distinguished. The number of evaluated points (n) as well as the mean values of c lattice parameter, length and thickness are provided at the upper left of the plots.

as it has been described earlier in murine healing bone (Hoerth et al., 2018). The mean Ca content of the callus (~23 wt%) is comparable to data presented by Haffner-Luntzer et al. (2016), who used a similar animal model and osteotomy stabilization method. Mineral particles located in these woven regions exhibit a low degree of orientation and are relatively thick but short, which is characteristic for woven bone (Hoerth et al., 2018; Kerschnitzki et al., 2011b, 2011a). These woven areas form at an early stage of mineralization in the callus region and presumably serve as a scaffold for the deposition of lamellar bone (Kerschnitzki et al., 2011a). The lamellar areas in callus bone exhibit typical mineral characteristics (Hoerth et al., 2018), i.e. a relatively high degree of orientation. The areas close to lacunae typically exhibit high T parameters and a relatively high degree of mineral platelet orientation (Fig. S4). The average lacunar density (Lc.N/TV $\approx 100 * 10^3$ mm^{-3}) and average lacunar volume (Lc.V $\approx$ 290 µm^3) are both significantly higher than in the cortical region. Lacunae properties in callus tissue are rarely studied so far, but Hernandez et al. reported two-dimensional data on rat bone and also found higher lacunar density in woven bone areas of the callus compared to the cortical bone (Hernandez et al. 2004).

By using qBEI we were able to identify cortex fragments (within the callus region) remaining from the osteotomy procedure, which did not show any rhodamine staining of the LCN. The absence of stained canaliculi here could be caused by sealing of the surface through macrophages and osteoclasts, which are assumed to secrete osteopontin onto calcified surfaces to inhibit extracellular bone resorption or phagocytosis (Dodds et al., 2009; McKee et al., 2011).

Calcified cartilage areas in the investigated callus tissue exhibit a very heterogeneous Ca content, and the mineral particles are small and rather randomly organized as compared to the other tissue types. The initially cartilaginous callus serves to stabilize the fracture site and vascularity progresses in the increasingly stable environment deeper into the callus (Shapiro, 2008). Woven bone is then synthesized on calcified cartilage cores of the callus and later cartilage transforms to bone by endochondral mechanisms. The so-called cartilage canals carrying blood vessels deep into the connective tissue could explain the high staining level of the cartilage by rhodamine. Blood vessels play an important role in the development, growth and removal of cartilage and forming bone by transporting fibroblasts and chondroclasts (Hall, 2015; Shipov et al., 2013). In addition, some areas within the bony callus have been identified as calcified cartilage islands (see Fig. 3, MF1 [ii]) and exhibit a positive correlation between T and ρ parameter as well as a relatively high Ca content. Lacunae located around these islands possess only few canaliculi. In general, calcified cartilage possibly plays an important mechanical role as a junction between two materials of very different stiffness, bone and unmineralized cartilage. We can infer that the characteristics found in the cartilage regions (low degree of organization, heterogeneous Ca content and small mineral particles) may indicate a different mechanical competence of this region compared to other mineralized regions.

As the fracture healing model represents different tissue types within a rather small sample volume, our data allows to characterize interfaces and transition zones between tissues as well as to discuss potential mechanisms of how these tissues develop and are structurally related to each other. We found significant differences in the lacunae density, lacunae volume and shape between cortical region and callus. The callus exhibits on average 34% higher lacunae number density and 40% larger lacunae than the cortical region. Although the lacunar volume (Lc.V) values from the bulk regions of the cortical region (151 ± 55 µm^3) and callus (290 ± 177 µm^3) on average approach each other within the transition zone, we find discontinuities around the interface (cortical region near interface: 197 ± 93 µm^3; callus near

interface: 327 ± 187 μm^3) (Fig. 6a). The oblateness shows a rather continuous transition across the interface (Fig. 6b). At the same time, the particle thickness and the calcium content decrease toward the cortex edges, which was also observed by Liu et al. (Liu et al., 2010). This might indicate a potential role of the osteocytes in dissolving parts of the cortical mineral phase by remodeling their environment to provide calcium and phosphate for the mineralization of the new formed callus similar to the reported effect during lactation in mice (Qing et al., 2012).

In general, lacunar volume and density depend on the corresponding tissue type, but also on animal and tissue age. A majority of studies indicate a reduction in osteocyte cell volume during aging that may be combined with reduced lacunar size aging (Tiede-Lewis and Dallas, 2019). The lacunar volume was reported to decrease with age in mouse bone (Hemmatian et al., 2018) as well as in human bone (Milovanovic et al., 2017). Although the mice in our study were older (26 weeks) compared to the mice of the above-mentioned studies (~16 weeks), ageing effects would not be sufficient to explain systematic differences in lacunar size. However, it still is under debate whether these changes also affect osteocyte mechanosensation. There is evidence that lacunar shape reflects the shape of the osteocyte within the lacuna (Vatsa et al., 2008) and that rounder osteocytes are more mechanosensitve (Bacabac et al., 2008). Finite element models suggest that the perilacunar environment is directly linked to the strain experienced by the osteocytes and that reduced lacunar size leads to a decreased mechanoreaction (Kola et al., 2020). Variations in lacunar density might also be caused by the higher activity of osteoblasts in the earlier stages of the bone healing process compared to the intramembranous growth process of the cortex (Hernandez et al., 2004). Furthermore, the size of osteocytes and related lacunae is suggested to be correlated to the size of osteoblasts before differentiation to osteocytes (Boyde, 1980) and also their deposition rate (Buenzli, 2015). The programmed cell death (apoptosis) of osteocytes is proposed to instruct neighboring viable osteocytes to synthesize cytokines, which then recruit osteoclasts to remove the dead cells and initiate remodeling of the surrounding matrix (Jilka et al., 2013; Verborgt et al., 2000). Therefore, a high lacunar density, i.e. high osteocyte density, as we find it in the callus woven bone, could potentially promote tissue removal and replacement by lamellar bone with a lower cell density (Vashishth et al., 2002). Thus, the osteocyte number may be an indicator for the bone turnover rate (Canè et al., 1982; Qiu et al., 2002) and may explain the transient nature of the woven bone callus.

Recently, synchrotron-based phase-contrast μCT was used to investigate human jawbone, revealing a direct correlation of its remodeling rate with the lacunar density and an inverse correlation with the local bone mineral density (Ca content) (Iezzi et al., 2020). We find a similar correlation, i.e. higher lacunar density in woven bone corresponding to a lower Ca content as compared to cortical tissue. The higher mean volume of lacunae and higher average lacunar density in the callus than in the cortical region presumably has an influence on the respective mechanical properties. Correlations between the mechanical behavior and the lacunar volume as well as lacunar density have been shown earlier (Yeni et al., 2001) and in addition it was reported that the callus stiffness during the late healing stages is only 70–60% of the cortex stiffness (Hoerth et al., 2018; Manjubala et al., 2009).

Besides the density and shape of lacunae, also the connections between them (canaliculi, housing the osteocyte processes), are indicators for the course of bone development. From the visualization of the LCN by CLSM, we see that canaliculi within the callus do not show a preferred orientation, while the canaliculi in the cortical region are preferentially oriented perpendicular to the longitudinal axis of the femur. We see a disruption of the majority of canaliculi across the interfaces between callus and the cortical region, although some canaliculi traverse this area. It has been suggested that the canaliculi may mediate between the injured bone matrix and the lamellar bone during ossification, and are therefore essential for new bone formation (Kusuzaki et al., 2000).

Mineral particle length and thickness in mice are known to increase with animal age (Lange et al., 2011). We observe a similar trend across the transition zone from callus (younger) to cortical (older) tissue, where the mineral particle dimensions increase (Fig. 8) as a function of tissue age. Within the transition zone we find a decrease of T parameter values at the cortical edges towards the callus tissue (Fig. 7a), indicating an influence on the particle size even in cortical bone by callus formation. While the T parameter and the c lattice constant vary in bony callus and calcified cartilage, the L parameter, i.e. the length of the mineral crystals, stays mainly at a small range around 19 nm – equivalent to the crystal size of fetal bone (Lange et al., 2011). This may indicate that the mineral particles first grow in thickness and lengthen only later. The crystal length (L parameter) as measured by x-ray scattering methods usually appears shorter (~15 – 25 nm) as compared to measurements of the particle length using electron microscopy (Ascenzi et al., 1965; Boyde and Jones, 1998). Within the callus tissue we also find position-dependent differences of mineral shapes, i.e. a change from short and thick to long and thin with increasing callus tissue age which is comparable to findings of Hoerth et al. in rodents (2018, 2014). This shape change was interpreted as contributing factor to stiffen the mineralized tissue with healing progression time (Hoerth et al., 2018; Manjubala et al., 2009) in accordance with theoretical predictions of mechanical behavior depending on the arrangement and shape of the mineral particles embedded in the collagen matrix (Jäger and Fratzl, 2000). This may be a possible explanation why the less organized woven bone tissues are replaced with higher organized lamellar tissue.

Changes in crystallographic parameters of the hydroxyapatite crystals allow an interpretation of the degree of carbonatization, i.e. the substitution of phosphate by carbonate (Handschin and Stern, 1995), and to some degree an interpretation of tissue maturation. The intercalation of trace elements and hydration also lead to a distortion of the crystal, i.e. changes in the lattice constant. In our samples, the c-lattice constant of hydroxyapatite and the particle length (L parameter) are linearly correlated if plotted for all tissue types (Fig. 8a). Across the transition zone at the callus-cortex interface we find a continuous increase of the c-lattice constant from the fracture-induced tissues (cartilage and bony callus) towards cortical bone. Something similar was observed in human teeth (Forien et al., 2016), where the decrease in c lattice parameter from outer (cementum) to later-formed inner regions (pulp) has been interpreted as a reduction in the apatite carbonate content as a function of root maturation. At the mineralization front of osteonal remodeling in human bone an analogous trend has been identified, i.e. at the mineralization front the lattice constant was found to be smaller than in the bulk tissue (Roschger et al., 2020). In our samples this would correspond to a lower carbonate content in the younger callus and cartilage regions as compared to the older cortical bone regions.

Based on these characteristics of mineral structure and LCN architecture across all tissue types and the corresponding transition zones, our study allows to draw some general –partly speculative– conclusions regarding bone development during fracture healing: (i) mineralized tissue regions serve consecutively as scaffolds for the next step in tissue formation (Kerschnitzki et al., 2011a). The osteotomy gap in the cortical tissue defines the position of mineralizing repair cartilage serving as base for the formation of woven bone, which then acts as scaffold for lamellar-like bone regions within the callus. (ii) Interfaces between tissues appear at different length scales, but we can speculate that the formation patterns at all transition zones depend mostly on mechanical conditions: early formed tissues are laid down quickly but with lower degrees of organization; later ones have higher degrees of organization and therefore probably show different mechanical properties. (iii) Porosities (lacunae and canaliculi as well as vascular channels) within the tissues are fingerprints of the endochondral bone formation mechanisms: lacunar shape and density indicate formation or remodeling

rates, while canalicular connectivity may indicate communication between cells across interfaces.

4.1. Limitations and specific characteristics of our study

We want to mention the following limitations and specific characteristics of our study. Although the observed healing progress was different in different animals, the same general principles of bone fracture healing were encountered. The healing process in some of the investigated samples could have been influenced by surgical procedures and debris from the Gigli saw, which could have led to increased inflammation (Wataha et al., 2001). Additionally, the heterogeneity in healing is affected by the interfragmentary movement within the fracture region. Interfragmentary movement is influenced strongly by the load on the operated limb due to gravity, muscle forces, and even the fixation stiffness used to stabilize the fracture. Presumably, all of these factors were similar within the study, although activity levels of the mice in the cages were not measured. Even other studies that reported better healing outcomes than those observed in the current study (Hoerth et al., 2018; Kruck et al., 2018; Röntgen et al., 2010), show very similar structural features as the samples in our study. Therefore, the discussed structural features are assumed to be representative for the respective tissue types. The study was based on five mice which underwent the surgical procedure and one control sample, taking into consideration all ethical issues. In the following, three osteotomized samples were selected and representative regions were investigated from the following number of samples by qBEI (longitudinal cross sections from all samples), CLSM (eleven regions from four samples), SAXS/WAXS (five regions from four samples) and μCT (two samples). Future investigations with this osteotomy model in skeletally mature mice will be extended to 28 days, to allow one more week for additional time of healing.

To assess potential participation of osteocytes in mineralization processes during healing, the mineral particle parameter maps are compared with CLSM and qBEI of the samples. Although the measurements of CLSM and qBEI were done on thick blocks, while the scanning SAXS/WAXS experiments were performed on thin slices, which were cut before the measurements, the respective sample regions still show comparable structural patterns. But the variations appear in different volume elements. Therefore, only qualitative correlations between the results of these methods can be reported. Nonetheless, the surroundings of large soft tissue regions (i.e. vascular channels) as well as positions of lacunae could be easily identified in the respective maps of mineral particle thickness and could be used for image registration.

5. Conclusions

Bone tissue organization constantly changes during the process of fracture healing. Consequently, various structures at all levels of hierarchy, cell geometry and mechanical properties can be observed at different sites across the healing bone. We demonstrated characteristic structural differences relating to the amount, orientation and shape of both mineral particles at the nanometer scale and lacunae at the micrometer length-scale across several tissue types and the interface between the cortical region and bony callus. The transition zone around the interface between cortical and callus regions showed a continuous convergence of mineral particle characteristics and lacunae shape, but the mean volume of lacunae in the callus tissue was approximately 40% larger than those found in the cortical tissue. Further studies are required to explain the reason for these size differences. To judge effects on mechanosensing amongst osteocytes in enlarged lacunae, future studies including measurements of osteocyte size similar to Tiede-Lewis et al. (2017) as well as load-induced fluid flow that can be sensed by the cells would be required. The majority of canaliculi between callus and cortical region were disrupted, while some were able to pass the transition zone, indicating a potential communication between osteocytes of both tissues. One could speculate that the increase in mineral particle parameter values in perilacunar regions of the callus could also be an indication of an osteocytic influence on the mineralization (Kerschnitzki et al., 2013). In our study also other presented correlations between LCN architecture and mineral characteristics, such as the inverse correlation of T parameter (low in callus vs. high in the cortical region) and lacunar density (high in callus vs. low in the cortical region) across the callus-cortex transition, could be a sign that osteocytes might be actively involved in the mineralization processes during healing. Further studies may lead to a deeper understanding of the mechanisms involved in osteocyte-mediated mineralization and would be essential for identifying new therapeutic strategies to support the bone healing process after injuries or surgeries.

CRediT authorship contribution statement

Victoria Schemenz: Writing - original draft, Visualization, Writing - review & editing. **André Gjardy:** Investigation, Visualization, Writing - review & editing. **Fereshteh F. Chamasemani:** Visualization, Writing - review & editing. **Andreas Roschger:** Investigation, Writing - review & editing. **Paul Roschger:** Investigation, Writing - review & editing. **Paul Zaslansky:** Investigation, Writing - review & editing. **Lukas Helfen:** Investigation, Writing - review & editing. **Manfred Burghammer:** Investigation, Writing - review & editing. **Peter Fratzl:** Supervision, Writing - review & editing. **Richard Weinkamer:** Conceptualization, Writing - review & editing. **Roland Brunner:** Investigation, Writing - review & editing. **Bettina M. Willie:** Conceptualization, Supervision, Resources, Writing - review & editing. **Wolfgang Wagermaier:** Conceptualization, Project administration, Funding acquisition, Supervision, Writing - review & editing.

Declaration of Competing Interest

The authors declare that they have no known competing financial interests or personal relationships that could have appeared to influence the work reported in this paper.

Acknowledgements

We thank I. Schmidt, B. Schonert, C. Li, S. Siegel, T. Grünewald, K. Klaushofer, P. Keplinger, S. Lueger, P. Messmer for their support and acknowledge the European Synchrotron Radiation Facility (ESRF) in Grenoble, France for granting us beamtime. We thank A. Seliger, C. Julien, and especially C. Figge, for performing the osteotomy surgeries. This study was supported by the German Research Foundation (Deutsche Forschungsgemeinschaft – Projektnummer 272944896), the DFG funding through the Berlin-Brandenburg School for Regenerative Therapies GSC 203, the COMET program within the K2 Center “Integrated Computational Material, Process and Product Engineering (IC-MPPE)” (Project No 859480) and the Shriners Hospital for Children and the FRQS Programme de bourses de chercheur (BMW).

Appendix A. Supplementary data

Supplementary data to this article can be found online at https://doi.org/10.1016/j.jsb.2020.107616.

References

Al-Aql, Z.S., Alagl, A.S., Graves, D.T., Gerstenfeld, L.C., Einhorn, T.A., 2008. Molecular mechanisms controlling bone formation during fracture healing and distraction osteogenesis. J. Dent. Res. 87, 107–118. https://doi.org/10.1177/154405910808700215.

Ascenzi, A., Bonucci, E., Steve Bocciarelli, D., 1965. An electron microscope study of osteon calcification. J. Ultrasructure Res. 12, 287–303. https://doi.org/10.1016/S0022-5320(65)80100-9.

Bacabac, R.G., Mizuno, D., Schmidt, C.F., Mackintosh, F.C., Loon, J.J.W.A.V., Klein-

Nulend, J., Smit, T.H., 2008. Round versus flat: bone cell morphology, elasticity, and mechanosensing. J. Biomech. 41, 1590–1598. https://doi.org/10.1016/j.jbiomech.2008.01.031.
Bach-Gansmo, F.L., Irvine, S.C., Brüel, A., Thomsen, J.S., Birkedal, H., 2013. Calcified cartilage islands in rat cortical bone. Calcif. Tissue Int. 92, 330–338. https://doi.org/10.1007/s00223-012-9682-6.
Bach-Gansmo, F.L., Weaver, J.C., Jensen, M.H., Leemreize, H., Mader, K.S., Stampanoni, M., Brüel, A., Thomsen, J.S., Birkedal, H., 2015. Osteocyte lacunar properties in rat cortical bone: differences between lamellar and central bone. J. Struct. Biol. 191, 59–67. https://doi.org/10.1016/j.jsb.2015.05.005.
Bach-Gansmo, F.L., Wittig, N.K., Brüel, A., Thomsen, J.S., Birkedal, H., 2016. Immobilization and long-term recovery results in large changes in bone structure and strength but no corresponding alterations of osteocyte lacunar properties. Bone 91, 139–147. https://doi.org/10.1016/j.bone.2016.07.005.
Benecke, G., Wagermaier, W., Li, C., Schwartzkopf, M., Flucke, G., Hoerth, R., Zizak, I., Burghammer, M., Metwalli, E., Müller-Buschbaum, P., Trebbin, M., Förster, S., Paris, O., Roth, S.V., Fratzl, P., 2014. A customizable software for fast reduction and analysis of large X-ray scattering data sets: applications of the new DPDAK package to small- angle X-ray scattering and grazing-incidence small- angle X-ray scattering. J. Appl. Cryst 47, 1797–1803. https://doi.org/10.1107/S1600576714019773.
Boyde, A., 1980. Evidence against Osteocytic osteolysis. Metab Bone Dis Rel Res 2, 239–255.
Boyde, A., Jones, S.B.T., 1998. Aspects of Anatomy and Development of Bone: the nm, μm and mm Hierarchy, in: Molecular and Cellular Biology of Bone – Advances in Organ Biology, Elsevier, pp. 3–44. https://doi.org/https://doi.org/10.1016/S1569-2590(08)60106-8.
Buenzli, P.R., 2015. Osteocytes as a record of bone formation dynamics: a mathematical model of osteocyte generation in bone matrix. J. Theor. Biol. 364, 418–427. https://doi.org/10.1016/j.jtbi.2014.09.028.
Burr, D.B., Allen, M.R., 2019. Basic and Applied Bone Biology. Academic Press.
Canè, V., Marotti, G., Volpi, G., Zaffe, D., Palazzini, S., Remaggi, F., Muglia, M.A., 1982. Size and density of osteocyte lacunae in different regions of long bones. Calcif. Tissue Int. 34, 558–563. https://doi.org/10.1007/BF02411304.
Currey, J.D., 2006. Bones: Structure and Mechanics. Princeton University Pres, New Jersey.
Danilchenko, S.N., Kukharenko, O.G., Moseke, C., Protsenko, I.Y., Sukhodub, L.F., Sulkio-Cleff, B., 2002. Determination of the bone mineral crystallite size and lattice strain from diffraction line broadening. Cryst. Res. Technol. 37, 1234–1240.
Dierolf, M., Menzel, A., Thibault, P., Schneider, P., Kewish, C.M., Wepf, R., Bunk, O., Pfeiffer, F., 2010. Ptychographic X-ray computed tomography at the nanoscale. Nature 467, 436–439. https://doi.org/10.1038/nature09419.
Dimitriou, R., Tsiridis, E., Giannoudis, P.V., 2005. Current concepts of molecular aspects of bone healing. Injury 36, 1392–1404. https://doi.org/10.1016/j.injury.2005.07.019.
Dodds, R.A., Connor, J.R., James, I.E., Lee Rykaczewski, E., Appelbaum, E., Dul, E., Gowen, M., 2009. Human osteoclasts, not osteoblasts, deposit osteopontin onto resorption surfaces: an in vitro and ex vivo study of remodeling bone. J. Bone Miner. Res. 10, 1666–1680. https://doi.org/10.1002/jbmr.5650101109.
Dong, P., Haupert, S., Hesse, B., Langer, M., Gouttenoire, P.-J., Bousson, V., Peyrin, F., 2014. 3D osteocyte lacunar morphometric properties and distributions in human femoral cortical bone using synchrotron radiation micro-CT images. Bone 60, 172–185. https://doi.org/10.1016/j.bone.2013.12.008.
Forien, J.B., Zizak, I., Fleck, C., Petersen, A., Fratzl, P., Zolotoyabko, E., Zaslansky, P., 2016. Water-mediated collagen and mineral nanoparticle interactions guide functional deformation of human tooth dentin. Chem. Mater. 28, 3416–3427. https://doi.org/10.1021/acs.chemmater.6b00811.
Franz-Odendaal, T.A., Hall, B.K., Witten, P.E., 2006. Buried alive: how osteoblasts become osteocytes. Dev. Dyn. 235, 176–190. https://doi.org/10.1002/dvdy.20603.
Fratzl, P., 1994. Statistical model of the habit and arrangement of mineral crystals in the collagen of bone. J. Stat. Phys. 77, 125–143.
Fratzl, P., Gupta, H.S., Paschalis, E.P., Roschger, P., 2004. Structure and mechanical quality of the collagen–mineral nano-composite in bone. J. Mater. Chem. 14, 2115–2123. https://doi.org/10.1039/B402005G.
Fratzl, P., Weinkamer, R., 2007. Nature's hierarchical materials. Prog. Mater Sci. 52, 1263–1334. https://doi.org/10.1016/j.pmatsci.2007.06.001.
Gerstenfeld, L.C., Alkhiary, Y.M., Krall, E.A., Nicholls, F.H., Stapleton, S.N., Fitch, J.L., Bauer, M., Kayal, R., Graves, D.T., Jepsen, K.J., Einhorn, T.A., 2006. Three-dimensional reconstruction of fracture callus morphogenesis. J. Histochem. Cytochem. 54, 1215–1228. https://doi.org/10.1369/jhc.6A6959.2006.
Goldstein, J.I., Newbury, D.E., Michael, J.R., Ritchie, N.W.M., Henry, J., Scott, J., Joy, D.C., 2018. In: Scanning Electron Microscopy and X-Ray Microanalysis, fourth ed. Springer, New York. https://doi.org/10.1007/978-1-4939-6676-9.
Haffner-Luntzer, M., Heilmann, A., Heidler, V., Liedert, A., Schinke, T., Amling, M., Yorgan, T.A., vom Scheidt, A., Ignatius, A., 2016. Hypochlorhydria-induced calcium malabsorption does not affect fracture healing but increases post-traumatic bone loss in the intact skeleton. J. Orthop. Res. 34, 1914–1921. https://doi.org/10.1002/jor.23221.
Hall, B.K., 2015. Vertebrate Cartilages, in: Bones and Cartilage. Elsevier, London, pp. 43–59. https://doi.org/10.1016/B978-0-12-416678-3.00003-3.
Han, Z., Bhavsar, M., Leppik, L., Oliveira, K.M.C., Barker, J.H., 2018. Histological scoring method to assess bone healing in critical size bone defect models. Tissue Eng. Part C Methods 24, 272–279. https://doi.org/10.1089/ten.tec.2017.0497.
Handschin, R.G., Stern, W.B., 1995. X-ray diffraction studies on the lattice perfection of human bone apatite (Crista Iliaca). Bone 16, 355S–363S. https://doi.org/10.1016/S8756-3282(95)80385-8.
Hemmatian, H., Laurent, M.R., Bakker, A.D., Vanderschueren, D., Klein-Nulend, J., van Lenthe, G.H., 2018. Age-related changes in female mouse cortical bone microporosity. Bone 113, 1–8. https://doi.org/10.1016/j.bone.2018.05.003.
Hernandez, C.J.J., Majeska, R.J.J., Schaffler, M.B.B., 2004. Osteocyte density in woven bone. Bone 35, 1095–1099. https://doi.org/10.1016/j.bone.2004.07.002.
Hesse, B., Varga, P., Langer, M., Pacureanu, A., Schrof, S., Männicke, N., Suhonen, H., Maurer, P., Cloetens, P., Peyrin, F., Raum, K., 2015. Canalicular network morphology is the major determinant of the spatial distribution of mass density in human bone tissue: evidence by means of synchrotron radiation phase-contrast nano-CT. J. Bone Miner. Res. 30, 346–356. https://doi.org/10.1002/jbmr.2324.
Heveran, C.M., Rauff, A., King, K.B., Carpenter, R.D., Ferguson, V.L., 2018. A new open-source tool for measuring 3D osteocyte lacunar geometries from confocal laser scanning microscopy reveals age-related changes to lacunar size and shape in cortical mouse bone. Bone 110, 115–127. https://doi.org/10.1016/j.bone.2018.01.018.
Hoerth, R.M., Kerschnitzki, M., Aido, M., Schmidt, I., Burghammer, M., Duda, G.N., Fratzl, P., Willie, B.M., Wagermaier, W., 2018. Correlations between nanostructure and micromechanical properties of healing bone. J. Mech. Behav. Biomed. Mater. 77, 258–266. https://doi.org/10.1016/j.jmbbm.2017.08.022.
Hoerth, R.M., Seidt, B.M., Shah, M., Schwarz, C., Willie, B.M., Duda, G.N., Fratzl, P., Wagermaier, W., 2014. Mechanical and structural properties of bone in non-critical and critical healing in rat. Acta Biomater. 10, 4009–4019. https://doi.org/10.1016/j.actbio.2014.06.003.
Holmbeck, K., Bianco, P., Pidoux, I., Inoue, S., Billinghurst, R.C., Wu, W., Chrysovergis, K., Yamada, S., Birkedal-Hansen, H., Poole, A.R., 2005. The metalloproteinase MT1-MMP is required for normal development and maintenance of osteocyte processes in bone. J. Cell Sci. 118, 147–156. https://doi.org/10.1242/jcs.01581.
Iezzi, G., Mangano, C., Barone, A., Tirone, F., Baggi, L., Tromba, G., Piattelli, A., Giuliani, A., 2020. Jawbone remodeling: a conceptual study based on synchrotron high-resolution tomography. Sci. Rep. 10, 1–12. https://doi.org/10.1038/s41598-020-60718-8.
Ip, V., Toth, Z., Chibnall, J., McBride-Gagyi, S., 2016. Remnant woven bone and calcified cartilage in mouse bone: differences between ages/sex and effects on bone strength. PLoS ONE 11, 1–15. https://doi.org/10.1371/journal.pone.0166476.
Jäger, I., Fratzl, P., 2000. Mineralized collagen fibrils: a mechanical model with a staggered arrangement of mineral particles. Biophys. J. 79, 1737–1746. https://doi.org/10.1016/S0006-3495(00)76426-5.
Jilka, R.L., Noble, B., Weinstein, R.S., 2013. Osteocyte apoptosis. Bone 54, 264–271. https://doi.org/10.1016/j.bone.2012.11.038.
Kerschnitzki, M., Kollmannsberger, P., Burghammer, M., Duda, G.N., Weinkamer, R., Wagermaier, W., Fratzl, P., 2013. Architecture of the osteocyte network correlates with bone material quality. J. Bone Miner. Res. 28, 1837–1845. https://doi.org/10.1002/jbmr.1927.
Kerschnitzki, M., Wagermaier, W., Liu, Y., Roschger, P., Duda, G.N., Fratzl, P., 2011a. Poorly ordered bone as an endogenous scaffold for the deposition of highly oriented lamellar tissue in rapidly growing ovine bone. Cells. Tissues. Organs 194, 119–123. https://doi.org/10.1159/000324467.
Kerschnitzki, M., Wagermaier, W., Roschger, P., Seto, J., Shahar, R., Duda, G.N., Mundlos, S., Fratzl, P., 2011b. The organization of the osteocyte network mirrors the extracellular matrix orientation in bone. J. Struct. Biol. 173, 303–311. https://doi.org/10.1016/J.JSB.2010.11.014.
Kieffer, J., Wright, J.P., 2013. PyFAI: a python library for high performance azimuthal integration on GPU. Powder Diffr. 28, 339–350. https://doi.org/10.1017/S0885715613000924.
Kola, S.K., Begonia, M.T., Tiede-Lewis, L.A.M., Laughrey, L.E., Dallas, S.L., Johnson, M.L., Ganesh, T., 2020. Osteocyte lacunar strain determination using multiscale finite element analysis. Bone Reports 12, 100277. https://doi.org/10.1016/j.bonr.2020.100277.
Kruck, B., Zimmermann, E.A., Damerow, S., Figge, C., Julien, C., Wulsten, D., Thiele, T., Martin, M., Hamdy, R., Reumann, M.K., Duda, G.N., Checa, S., Willie, B.M., 2018. Sclerostin neutralizing antibody treatment enhances bone formation but does not rescue mechanically induced delayed healing. J. Bone Miner. Res. 33, 1686–1697. https://doi.org/10.1002/jbmr.3454.
Kusuzaki, K., Kageyama, N., Shinjo, H., Takeshita, H., Murata, H., Hashiguchi, S., Ashihara, T., Hirasawa, Y., 2000. Development of bone canaliculi during bone repair. Bone 27, 655–659. https://doi.org/10.1016/S8756-3282(00)00383-5.
Lange, C., Li, C., Manjubala, I., Wagermaier, W., Kühnisch, J., Kolanczyk, M., Mundlos, S., Knaus, P., Fratzl, P., 2011. Fetal and postnatal mouse bone tissue contains more calcium than is present in hydroxyapatite. J. Struct. Biol. 176, 159–167. https://doi.org/10.1016/j.jsb.2011.08.003.
Liu, Y., Manjubala, I., Schell, H., Epari, D.R., Roschger, P., Duda, G.N., Fratzl, P., 2010. Size and habit of mineral particles in bone and mineralized callus during bone healing in sheep. J. Bone Miner. Res. 25, 2029–2038. https://doi.org/10.1002/jbmr.84.
Mader, K.S., Schneider, P., Müller, R., Stampanoni, M., 2013. A quantitative framework for the 3D characterization of the osteocyte lacunar system. Bone 57, 142–154. https://doi.org/10.1016/j.bone.2013.06.026.
Manjubala, I., Liu, Y., Epari, D.R., Roschger, P., Schell, H., Fratzl, P., Duda, G.N., 2009. Spatial and temporal variations of mechanical properties and mineral content of the external callus during bone healing. Bone 45, 185–192. https://doi.org/10.1016/j.bone.2009.04.249.
Marsell, R., Einhorn, T.A., 2012. The biology of fracture healing. Injury 42, 551–555. https://doi.org/10.1016/j.injury.2011.03.031.
McKee, M.D., Pedraza, C.E., Kaartinen, M.T., 2011. Osteopontin and wound healing in bone. Cells Tissues Organs 194, 313–319. https://doi.org/10.1159/000324244.
Milovanovic, P., Zimmermann, E.A., vom Scheidt, A., Hoffmann, B., Sarau, G., Yorgan, T., Schweizer, M., Amling, M., Christiansen, S., Busse, B., 2017. The formation of calcified nanospherites during micropetrosis represents a unique mineralization

mechanism in aged human bone. Small 13, 1–10. https://doi.org/10.1002/smll.201602215.
Nefussi, J.R., Sautier, J.M., Nicolas, V., Forest, N., 1991. How osteoblasts become osteocytes: a decreasing matrix forming process. J. Biol. Buccale 19, 75–82.
Pabisch, S., Wagermaier, W., Zander, T., Li, C., Fratzl, P., 2013. Imaging the Nanostructure of Bone and Dentin Through Small- and Wide-Angle X-Ray Scattering, in: De Yoreo, J.J.B.T.-M. in E. (Ed.), Methods in Enzymology. Academic Press, San Diego, pp. 391–413. https://doi.org/https://doi.org/10.1016/B978-0-12-416617-2.00018-7.
Porod, G., 1951. Die Röntgenkleinwinkelstreuung von dichtgepackten kolloiden Systemen – I. Teil. Kolloid-Zeitschrift 124, 83–114. https://doi.org/10.1007/BF01512792.
Qing, H., Ardeshirpour, L., Divieti Pajevic, P., Dusevich, V., Jähn, K., Kato, S., Wysolmerski, J., Bonewald, L.F., 2012. Demonstration of osteocytic perilacunar/canalicular remodeling in mice during lactation. J. Bone Miner. Res. 27, 1018–1029. https://doi.org/10.1002/jbmr.1567.
Qiu, S., Rao, D., Palnitkar, S., Parfitt, A., 2002. Relationships between osteocyte density and bone formation rate in human cancellous bone. Bone 31, 709–711. https://doi.org/10.1016/S8756-3282(02)00907-9.
Repp, F., Kollmannsberger, P., Roschger, A., Berzlanovich, A., Gruber, G.M., Roschger, P., Wagermaier, W., Weinkamer, R., 2017. Coalignment of osteocyte canaliculi and collagen fibers in human osteonal bone. J. Struct. Biol. 199, 177–186. https://doi.org/10.1016/j.jsb.2017.07.004.
Reznikov, N., Shahar, R., Weiner, S., 2014. Bone hierarchical structure in three dimensions. Acta Biomater. 10, 3815–3826. https://doi.org/10.1016/j.actbio.2014.05.024.
Rinnerthaler, S., Roschger, P., Jakob, H.F., Nader, A., Klaushofer, K., Fratzl, P., 1999. Scanning small angle X-ray scattering analysis of human bone sections. Calcif. Tissue Int. 64, 422–429. https://doi.org/10.1007/PL00005824.
Röntgen, V., Blakytny, R., Matthys, R., Landauer, M., Wehner, T., Göckelmann, M., Jermendy, P., Amling, M., Schinke, T., Claes, L., Ignatius, A., 2010. Fracture healing in mice under controlled rigid and flexible conditions using an adjustable external fixator. J. Orthop. Res. 28, 1456–1462. https://doi.org/10.1002/jor.21148.
Roschger, A., Roschger, P., Wagermaier, W., Chen, J., van Tol, A.F., Repp, F., Blouin, S., Berzlanovich, A., Gruber, G.M., Klaushofer, K., Fratzl, P., Weinkamer, R., 2019. The contribution of the pericanalicular matrix to mineral content in human osteonal bone. Bone 123, 76–85. https://doi.org/10.1016/j.bone.2019.03.018.
Roschger, A., Wagermaier, W., Gamsjaeger, S., Hassler, N., Schmidt, I., Blouin, S., Berzlanovich, A., Gruber, G.M., Weinkamer, R., Roschger, P., Paschalis, E.P., Klaushofer, K., Fratzl, P., 2020. Newly formed and remodeled human bone exhibits differences in the mineralization process. Acta Biomater. 104, 221–230. https://doi.org/10.1016/j.actbio.2020.01.004.
Roschger, P., Fratzl, P., Eschberger, J., Klaushofer, K., 1998. Validation of quantitative backscattered electron imaging for the measurement of mineral density distribution in human bone biopsies. Bone 23, 319–326. https://doi.org/10.1016/S8756-3282(98)00112-4.
Roschger, P., Paschalis, E.P.P., Fratzl, P., Klaushofer, K., 2008. Bone mineralization density distribution in health and disease. Bone 42, 456–466. https://doi.org/10.1016/j.bone.2007.10.021.
Schindelin, J., Arganda-Carreras, I., Frise, E., Kaynig, V., Longair, M., Pietzsch, T., Preibisch, S., Rueden, C., Saalfeld, S., Schmid, B., Tinevez, J.-Y., White, D.J., Hartenstein, V., Eliceiri, K., Tomancak, P., Cardona, A., 2012. Fiji: an open-source platform for biological-image analysis. Nat. Methods 9, 676–682. https://doi.org/10.1038/nmeth.2019.
Schmidt-Bleek, K., Petersen, A., Dienelt, A., Schwarz, C., Duda, G.N., 2014. Initiation and early control of tissue regeneration – bone healing as a model system for tissue regeneration. Expert Opin. Biol. Ther. 14, 247–259. https://doi.org/10.1517/14712598.2014.857653.
Schneider, C.A., Rasband, W.S., Eliceiri, K.W., 2012. NIH Image to ImageJ: 25 years of image analysis. Nat. Methods 9, 671–675. https://doi.org/10.1038/nmeth.2089.
Schneider, P., Meier, M., Wepf, R., Müller, R., 2011. Serial FIB/SEM imaging for quantitative 3D assessment of the osteocyte lacuno-canalicular network. Bone 49, 304–311. https://doi.org/10.1016/j.bone.2011.04.005.
Schneider, P., Stauber, M., Voide, R., Stampanoni, M., Donahue, L.R., Müller, R., 2007. Ultrastructural properties in cortical bone vary greatly in two inbred strains of mice as assessed by synchrotron light based micro- and nano-CT. J. Bone Miner. Res. 22, 1557–1570. https://doi.org/10.1359/jbmr.070703.
Shapiro, F., 2008. Bone development and its relation to fracture repair. The role of mesenchymal osteoblasts and surface osteoblasts. Eur. Cells Mater. 15, 53–76. https://doi.org/10.22203/eCM.v015a05.
Shipov, A., Zaslansky, P., Riesemeier, H., Segev, G., Atkins, A., Shahar, R., 2013. Unremodeled endochondral bone is a major architectural component of the cortical bone of the rat (Rattus norvegicus). J. Struct. Biol. 183, 132–140. https://doi.org/10.1016/J.JSB.2013.04.010.
Tiede-Lewis, L.A.M., Dallas, S.L., 2019. Changes in the osteocyte lacunocanalicular network with aging. Bone 122, 101–113. https://doi.org/10.1016/j.bone.2019.01.025.
Tiede-Lewis, L.A.M., Xie, Y., Hulbert, M.A., Campos, R., Dallas, M.R., Dusevich, V., Bonewald, L.F., Dallas, S.L., 2017. Degeneration of the osteocyte network in the C57BL/6 mouse model of aging. Aging (Albany NY) 9, 2187–2205.
Tsourdi, E., Jähn, K., Rauner, M., Busse, B., Bonewald, L.F., 2018. Physiological and pathological osteocytic osteolysis 18, 292–303.
Vashishth, D., Gibson, G., Kimura, J., Schaffler, M.B., Fyhrie, D.P., 2002. Determination of bone volume by osteocyte population. Anat. Rec. 267, 292–295. https://doi.org/10.1002/ar.10114.
Vatsa, A., Breuls, R.G., Semeins, C.M., Salmon, P.L., Smit, T.H., Klein-Nulend, J., 2008. Osteocyte morphology in fibula and calvaria — is there a role for mechanosensing? Bone 43, 452–458. https://doi.org/10.1016/J.BONE.2008.01.030.
Verborgt, O., Gibson, G.J., Schaffler, M.B., 2000. Loss of osteocyte integrity in association with microdamage and bone remodeling after fatigue in vivo. J. Bone Miner. Res. 15, 60–67. https://doi.org/10.1359/jbmr.2000.15.1.60.
Voide, R., Schneider, P., Stauber, M., van Lenthe, G.H., Stampanoni, M., Müller, R., 2011. The importance of murine cortical bone microstructure for microcrack initiation and propagation. Bone 49, 1186–1193. https://doi.org/10.1016/j.bone.2011.08.011.
Vorauer, T., Kumar, Praveen Berhaut, C., Chamasemani, F.F., Jouneau, Pierre-Henri Aradilla, D., Tardif, S., Pouget, S., Fuchsbichler, B., Helfen, L., Selcuk, A., Widanage, Dhammika Koller, S., Lyonnard, Sandrine Brunner, R., 2020. Multi-scale quantification and modeling of aged nanostructured silicon-based composite anodes. Commun. Chem. accepted.
Wataha, J.C., O'Dell, N.L., Singh, B.B., Ghazi, M., Whitford, G.M., Lockwood, P.E., 2001. Relating nickel-induced tissue inflammation to nickel releasein vivo. J. Biomed. Mater. Res. 58, 537–544. https://doi.org/10.1002/jbm.1052.
Weinkamer, R., Kollmannsberger, P., Fratzl, P., 2019. Towards a connectomic description of the osteocyte lacunocanalicular network in bone. Curr. Osteoporos. Rep. 17, 186–194. https://doi.org/10.1007/s11914-019-00515-z.
Wittig, N.K., Laugesen, M., Birkbak, M.E., Bach-Gansmo, F.L., Pacureanu, A., Bruns, S., Wendelboe, M.H., Brüel, A., Sørensen, H.O., Thomsen, J.S., Birkedal, H., 2019. Canalicular junctions in the osteocyte lacuno-canalicular network of cortical bone. ACS Nano 13, 6421–6430. https://doi.org/10.1021/acsnano.8b08478.
Yeni, Y.N., Vashishth, D., Fyhrie, D.P., 2001. Estimation of bone matrix apparent stiffness variation caused by osteocyte lacunar size and density. J. Biomech. Eng. 123, 10–17. https://doi.org/10.1115/1.1338123.
Zhao, W., Byrne, M.H., Wang, Y., Krane, S.M., 2000. Osteocyte and osteoblast apoptosis and excessive bone deposition accompany failure of collagenase cleavage of collagen. J. Clin. Invest. 106, 941–949. https://doi.org/10.1172/JCI10158.
Zou, Z., Tang, T., Macías-Sánchez, E., Sviben, S., Landis, W.J., Bertinetti, L., Fratzl, P., 2020. Three-dimensional structural interrelations between cells, extracellular matrix, and mineral in normally mineralizing avian leg tendon. Proc. Natl. Acad. Sci. U. S. A. 117, 14102–14109. https://doi.org/10.1073/pnas.1917932117.